Modeling dispersal of the Pearl River-derived sediment over the Shelf

Guang Zhang[1,2,3], Suan Hu[1,2,3], Xiaolong Yu[1,2,3], Heng Zhang[1,2,3], Wenping Gong[1,2,3]*

[1] School of Marine Sciences, Sun Yat-sen University, Zhuhai, 519082, China

[2] Guangdong Provincial Key Laboratory of Marine Resources and Coastal Engineering, Zhuhai, 519082, China

[3] Pearl River Estuary Marine Ecosystem Research Station, Ministry of Education, Zhuhai 519082, China

Corresponding author: Wenping Gong (gongwp@mail.sysu.edu.cn)

Abstract

This study employs the Coupled Wave–Ocean–Sediment Transport Model to quantitatively assess the seasonal suspension, transport, and annual fate of Pearl River-derived sediment on the northern South China Sea (SCS) continental shelf. After careful model validation, several sensitivity model simulations were conducted. Results reveal pronounced seasonal variations in sediment dynamics driven by the monsoonal climate. During the wet summer, calm conditions favor initial deposition via the river plume, whereas stronger winter winds and waves resuspend and transport sediments into the Beibu Gulf. Spatially, 66.45% of the total sediment load is retained within the estuarine vicinity, 9.2% is deposited on the eastern continental shelf, and 8.86% and 10.3% accumulate in the Beibu Gulf and the area south of Hainan Island, respectively. Sensitivity experiments highlight the distinct roles of tidal forces, wave action, and background circulation in sediment transport and deposition. Tidal dynamics govern sediment behavior in the Pearl River Estuary, where neglecting tidal effects underestimates bottom shear stress, overestimates sediment deposition, and underestimates distal retention. Wave action dominates sediment resuspension at the river mouth, nearshore regions, particularly during high-energy winter periods. Excluding waves leads to overestimated deposition in these areas and underestimates accumulation in the Beibu Gulf. Background circulation is most influential in summer, with a strong northeastward current transporting sediments to the eastern shelf. Without this current, only 0.84% of sediments reach the eastern shelf, leading to an overestimation of distal deposition. The sediment model results are also highly

sensitive to sediment parameterization and initial conditions. Neglecting seasonal variations in critical shear stress for erosion overestimates winter resuspension and erosion east of the Leizhou Peninsula, increasing distal retention. Higher settling velocities lower SSC while overestimating proximal retention and underestimating distal retention. Additionally, initial sediment conditions significantly impact sediment transport, with the retention of pre-existing sediment leading to further offshore transport. However, the model is relatively insensitive to the initial bed grain size distribution. This study provides a comprehensive assessment of Pearl River-derived sediment dynamics and highlights key physical mechanisms governing sediment fate in the northern SCS.

Keywords

Riverine sediment transport; Sediment retention; Numerical modeling; Pearl River Estuary

1. Introduction

The transport process of suspended sediment from river source to ocean sink is an important link in the global material cycle (Kuehl et al., 2016;Liu et al., 2016;Cao et al., 2019). Much of the riverine sediment is trapped on the shallow shoals in estuaries, while the rest is transported by river plume out of the estuary (Meade, 1969;Burchard et al., 2018;Zhang et al., 2019). The riverine sediment carried by the river plume has a significant impact on the water quality, ecology, and geomorphology of the estuaries and continental shelves (Wright and Coleman, 1973;Turner and Millward, 2002).

The transport and deposition of riverine sediments from river source to estuarine,

54 coastal, and shelf environments are governed by various physical processes, including
55 tidal forces, wave action, and shelf circulation dynamics (Gao and Collins, 2014).
56 Tides play a critical role in estuarine sediment transport dynamics, as spring tides
57 typically produce higher bed shear stress, enhanced sediment resuspension, and
58 greater offshore sediment transport flux compared to neap tides (Bever and
59 MacWilliams, 2013;Zhang et al., 2019). In nearshore regions, wave-induced bed shear
60 stress is often an order of magnitude higher than that generated by currents (Xue et al.,
61 2012). Furthermore, wave-driven sediment resuspension frequently exceeds, and is
62 often several times greater than, the peak levels achieved by current-induced
63 resuspension (Sanford, 1994;Brand et al., 2010). In shelf regions, shelf circulations
64 significantly influence sediment transport, with the magnitude of along-shelf transport
65 substantially exceeding the cross-shelf component in most locations (Nittrouer and
66 Wright, 1994;Gao and Collins, 2014).

67 Furthermore, sediment properties, including settling velocity (Xia et al.,
68 2004;Chen et al., 2010;Cheng et al., 2013), critical shear stress for erosion (Dong et
69 al., 2020), and bed grain size distribution (Xue et al., 2012;Bever and MacWilliams,
70 2013), significantly influence sediment transport dynamics and
71 deposition/resuspension processes. Settling velocity can influence the location of
72 sediment depocenters, with higher settling velocities leading to more proximal
73 entrapment and vice versa (Ralston and Geyer, 2017). Similarly, critical shear stress
74 for erosion can affect the resuspension of deposited sediment, with higher critical
75 shear stress resulting in less resuspension and more deposition especially during neap

tides and weak wind wave periods (Dong et al., 2020;Choi et al., 2023).

A comprehensive understanding of sediment transport and deposition from river source to ocean sink requires the integrated consideration of both physical forcing factors and inherent sediment characteristics. Here, we present the transport and deposition of Pearl River-derived sediments on the continental shelf as a case study. The Pearl River, ranking as China's second-largest river in terms of freshwater discharge (Hu et al., 2011), forms the Pearl River Estuary (PRE) in its lower reaches (Figures 1 and S1). Its freshwater and sediment discharge are primarily delivered through eight major outlets (Figure S1b; Wu et al., 2016;Zhang et al., 2019), forming distinct plumes that extend across the northern South China Sea (SCS) shelf. The present average annual (2001-2022) freshwater and riverine sediment loads are 2.74×10^{11} m^3 and 2.84×10^7 tons, as reported by the Ministry of Water Resources of the People's Republic of China (http://www.mwr.gov.cn/sj/#tjgb). The distribution of these inputs shows significant seasonal variability: approximately 80% of the freshwater and 95% of the sediment load are transported during the wet summer season (April to September), while the remaining portion is discharged during the dry winter season (Xia et al., 2004).

The northern SCS, shaped by the East Asian Monsoon, displays marked seasonal contrasts, featuring winter monsoon winds averaging 7-10 m s^{-1} and summer winds typically below 6 m s^{-1} (Su, 2004;Ou et al., 2009). This seasonal shift drives coastal currents: northeastward in summer and southwestward in winter (Gan et al., 2009;Gan et al., 2013). Beyond the coastal zone, the consistent SCS Warm Current (SCSWC)

98 flows northeastward along the shelf break and inner continental slope toward the
99 Taiwan Strait, originating near Hainan Island and persisting year-round, even during
100 the winter northeast monsoon, across a remarkable distance of 600-700 km to the
101 southern tip of the Taiwan Strait (Su, 2004;Yang et al., 2008).

102 The PRE is situated in the central part of the northern South China Sea boundary,
103 positioned between the Taiwan Banks and Hainan Island. The PRE has a micro-tidal
104 and mixed semi-diurnal regime, with daily inequality in the range and in the time
105 between the high and low tides (Mao et al., 2004). The neap and spring tides
106 alternately influence the water elevation downstream of the estuary, with tidal ranges
107 varying from approximately 0.7 m during neap tides to over 2 m during spring tides
108 (Chen et al., 2016;Gong et al., 2018b). The PRE and the nearby shelf exhibit strong
109 seasonal variation in water column stability and are highly stratified during the wet
110 summer season, while the PRE becomes partially mixed or vertically well-mixed
111 during the dry winter season (Dong et al., 2004). Offshore of the PRE region, wave
112 conditions display distinct seasonal patterns: the waves are mild during summer, and
113 become stronger during winter, marked by larger southeasterly waves (Gong et al.,
114 2018a;Gong et al., 2018b;Zhang et al., 2021).

115 Previous studies have focused on sediment transport within the PRE. Most Pearl
116 River-derived sediments are deposited within the estuary, and neglecting tidal effects
117 can lead to overestimating deposition rates while underestimating offshore sediment
118 flux (Hu et al., 2011). The depositional dynamics of sediments from different PRE
119 outlets are shaped by outlet location, topography, and tidal conditions, with neap tides

120 favoring sediment accumulation on shoals and spring tides driving erosion and
121 enhancing offshore sediment transport (Zhang et al., 2019). Waves further intensify
122 both lateral trapping within the PRE and offshore sediment transport (Liu and Cai,
123 2019;Zhang et al., 2021).

124 However, numerical studies on the transport of Pearl River-derived sediments
125 across the continental shelf remain scarce, even amidst the widespread adoption of
126 computer modeling approaches. Previous research on the distribution of these
127 sediments has primarily relied on analyses of seismic profiles, gravity cores, and
128 laboratory-based radiometric dating of sediment samples (Ge et al., 2014;Liu et al.,
129 2014;Cao et al., 2019;Lin et al., 2020;Chen et al., 2023). Outside the PRE, gravity
130 core and seismic survey data were used to examine the Holocene sedimentary
131 processes, revealing two distinct mud depo-centers: an eastward proximal depo-center
132 extending southeastward and a southwestward distal mud belt (Ge et al., 2014;Liu et
133 al., 2014;Chen et al., 2023). However, seismic and drilling data cannot confirm that
134 the Pearl River sediment can be transported to the Beibu Gulf (Ge et al., 2014). Due to
135 the lack of sufficient gravity core samples and seismic data, it is difficult to
136 quantitatively attribute the sediment in the Beibu Gulf to the Pearl River-derived
137 sediment (Cao et al., 2019). Afterward, Lin et al. (2020) used the ^{226}Ra—^{238}U and
138 ^{232}Th—^{238}U endmembers model based on measurements of radionuclides in the
139 surface sediment samples. They found that approximately 15% of the surface
140 sediment in the nearshore area of the Beibu Gulf originates from the PRE region.
141 However, their studies only address the proportion of PRE sediment in the surface

142 sediment of the Beibu Gulf, without directly indicating the seasonal transport
143 pathways, flux, and annual deposition mechanisms of sediment from the Pearl River.
144 A gap persists in understanding how physical processes (such as tides, waves, and
145 ambient circulations) and sediment characteristics (such as critical shear stress for
146 erosion, settling velocity) and sediment initial conditions influence the seasonal
147 suspension, transport, and annual deposition of Pearl River-derived sediment on the
148 shelf. In this study, we utilize numerical modeling, complemented by extensive
149 collection of field observations and seabed grain size distribution data for model
150 calibration and validation—a highly effective approach for exploring mechanisms and
151 testing hypotheses derived from limited observational datasets. This study focused on
152 the processes of Pearl River-derived sediment suspension, transport, and deposition
153 over the continental shelf. Several specific questions addressed in this paper include:
154 (1) What are the seasonal dispersal and annual deposition patterns of the Pearl
155 River-derived sediment over the continental shelf?
156 (2) How do physical processes, sediment characteristics and sediment initial
157 conditions influence the dispersal of the Pearl River-derived sediment?
158

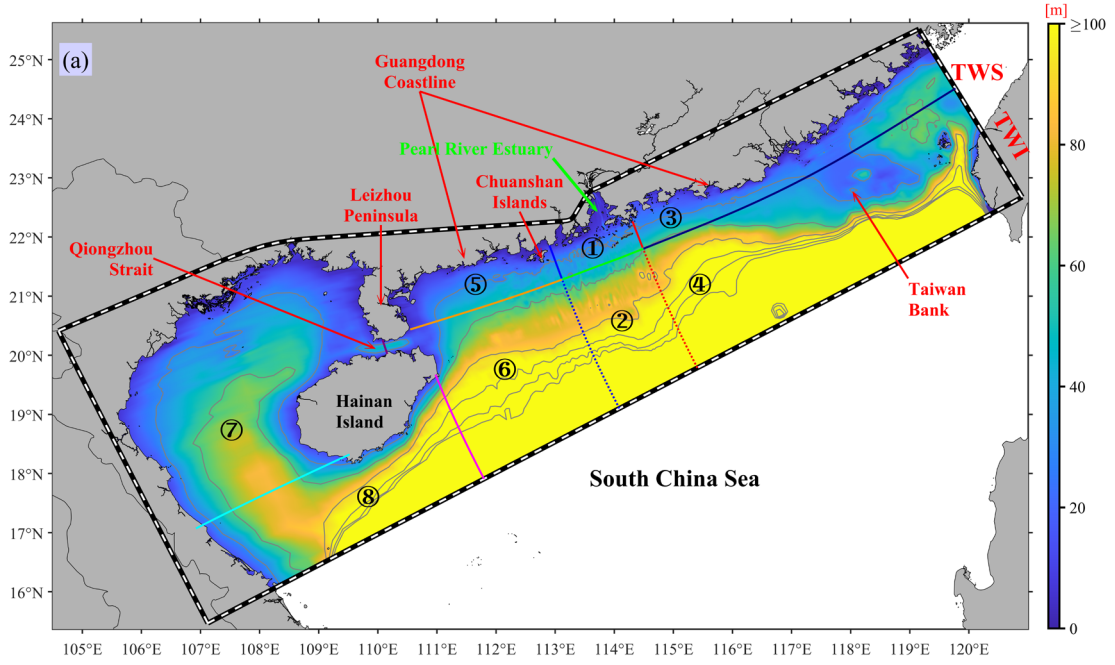

Figure 1. Bathymetry (shading) and isobath contours of the study area, with the ROMS/SWAN model grid domain outlined by black-to-white dashed lines. Circled numbers ①-⑧ denote the eight regions: Proximal, Southern, Eastern, Southeastern, Western, Southwestern, Beibu Gulf, and Distal regions, as defined by transects and detailed in Section 4.2. The abbreviations TWI and TWS mean Taiwan Island and Taiwan Strait, respectively. The gray contours represent 30-180 m isobaths at 30 m intervals, a consistent feature maintained in all subsequent figures that include these isobath contours.

2. Methods

2.1 Model coupling

This study employed the Coupled Ocean Atmosphere Wave Sediment Transport (COAWST, version 3.4) modeling system (Warner et al., 2005;Warner et al.,

2008;Warner et al., 2010), which includes a Model Coupling Toolkit (MCT) to facilitate data exchange among different modules (Jacob et al., 2005;Larson et al., 2005). The COAWST system consists of several modeling components, mainly comprises a hydrodynamic module (Regional Ocean Modeling System; ROMS) (Shchepetkin and McWilliams, 2005;Haidvogel et al., 2008), an atmospheric module (Advanced Research Weather Research and Forecasting; WRF) (Skamarock et al., 2005), a wave module (Simulating Waves Nearshore; SWAN) (Booij et al., 1999), and a sediment transport module (Community Sediment Transport Modeling System; CSTM) (Warner et al., 2008).

In this study, we established a coupling between ROMS, SWAN, and CSTM. The model grid covers the northern continental shelf of the South China Sea, including the PRE (Figure 1). The regional model was configured with 170 × 482 horizontal grid cells, with horizontal resolution varying from approximately 0.1 km near the PRE to about 10 km at outer open boundaries (Hu et al., 2024). The model grid bathymetry data was obtained from nautical charts compiled by the China Maritime Safety Administration and the General Bathymetric Chart of the Oceans (GEBCO) (Weatherall et al., 2015). The vertical grid used a Sigma coordinate system with 20 layers and a stretching transformation for higher resolution near the surface and bottom, with stretching parameters of θ_s=3.0 and θ_b=3.0, respectively (Song and Haidvogel, 1994). For model validations, please refer to the Supplementary Material (Supplement Figures S1-S10).

2.2 ROMS model setup

For the ROMS model, we utilized the Generic Length Scale turbulence closure scheme (Warner et al., 2005) for vertical turbulence parameterization. The method of Smagorinsky (1963) was employed to calculate the horizontal eddy viscosity and diffusivity. The Flather and Chapman boundary conditions were applied to barotropic current and water elevation at open boundaries, respectively (Flather, 1976;Chapman, 1985). Meanwhile, the open-boundary conditions for temperature, salinity, and sediment concentration were imposed by radiation methods (Orlanski, 1976;Raymond and Kuo, 1984). Surface forcing (including wind, net shortwave radiation, air temperature, atmospheric pressure, specific/relative humidity, and rain, etc.) data were sourced from the Climate Forecast System Reanalysis of the National Centers for Environmental Prediction (NCEP) (Saha et al., 2014), with a temporal resolution of 1 h and a spatial resolution of 0.3° × 0.3°. Water level and current open-boundary conditions comprised two components: tidal and subtidal. The tidal component was obtained from the Oregon State University Tidal Prediction Software database (Egbert and Erofeeva, 2002), while the subtidal component was interpolated from the HYbrid Coordinate Ocean Model (HYCOM) outputs (Chassignet et al., 2007).

2.3 Wave model setup

The SWAN model was executed and coupled to the same grid as the ROMS model (Warner et al., 2010). It was driven by surface atmospheric forces, real-time water level, and current fields from the ROMS and boundary reanalysis data. Wave boundary conditions were specified using nonstationary wave parameters from outputs of the NOAA WAVEWATCH III global ocean wave model solutions (Tolman

et al., 2016). Information was exchanged at 15-minute intervals to introduce wave-current interaction (WCI) between the ROMS and SWAN models (McWilliams et al., 2004;Kumar et al., 2012). This exchange included Hsig, surface peak wave period, mean wave direction and length, wave energy dissipation, and the percentage of breaking waves from SWAN to ROMS, as well as water level and current from ROMS to SWAN.

Additionally, the wave-current bottom boundary module based on Madsen (1994), incorporated into COAWST, was activated to simulate the wave-current bottom boundary layer. The vortex force module of wave forces was also activated to compute the wave-induced momentum flux, utilizing the method proposed by McWilliams et al. (2004) and implemented in COAWST by Kumar et al. (2012). The bottom friction was computed based on a logarithmic velocity profile (Warner et al., 2008).

2.4 Specifications of riverine input and sediment model

The freshwater discharge for the Pearl River was specified at the northern boundary using daily measured data from the Pearl River Water Resources Commission, while downstream precipitation within the Pearl River Basin was neglected. The full simulation model was initialized on the first day of January 2016 using temperature, salinity, and current fields interpolated from the HYCOM model, and it concluded on March 31, 2018. More than one year of hydrodynamic and sediment spin-up is sufficient to achieve appropriate seabed sediment particle size distribution, as well as stable circulation and thermohaline fields. This study primarily

analyzes the last 12 months, specifically from April 1, 2017, to March 31, 2018. This year is selected because the freshwater discharge and sediment load of the Pearl River closely approximate the average values of the past two decades, with a runoff of 3.35 $\times 10^{11}$ m^3 and a sediment load of 3.45 $\times 10^7$ tons, closely resembling the averages from 2001 to 2022.

Since the daily riverine sediment loads were unavailable, we modified the previous research results on sediment rating curves (Zhang et al., 2012) to suit for our study, as expressed by

$$y = 0.00002263x^{1.792} \quad (1)$$

where y is the Pearl River-derived suspended sediment concentration (mg L^{-1}), x is the Pearl River freshwater discharge rate (m^3 s^{-1}). Based on this relationship, the total amount of Pearl River sediment input over our 12-months study period (Fig. 3b) was 34.52 million tons, aligning closely with the annual load reported in 2017 by the Pearl River Water Resources Commission. The riverine sediment input, derived from the river discharge, was allocated across the eight outlets along the north boundary (Figure S1b) based on the distribution approach of Hu et al. (2011).The subsequent step involves establishing the proportion of seabed sediment particle size components. Sediments are typically categorized into three grain-size classes: clay (0-4 μm), silt (4-63 μm), and sand (63-2000 μm), as outlined by Shepard (1954). Data on sediment particle size composition for the northern continental shelf of the South China Sea and the PRE area were acquired through multiple voyage observations (Zhang et al., 2013;Zhang et al., 2019). Furthermore, publicly available data from published

literature were compiled (Gao et al., 2007;Kirby et al., 2008;Gao et al., 2010;Huang et al., 2013;Liu et al., 2014;Wang et al., 2014;Wang et al., 2015;Wang et al., 2016;Ge et al., 2017;Lu et al., 2017;Zhong et al., 2017;Yang et al., 2018;Ge et al., 2019). Finally, component distribution data for different particle size classes of seabed sediment were obtained from a total of 1981 measured stations (Figure 2a-c).

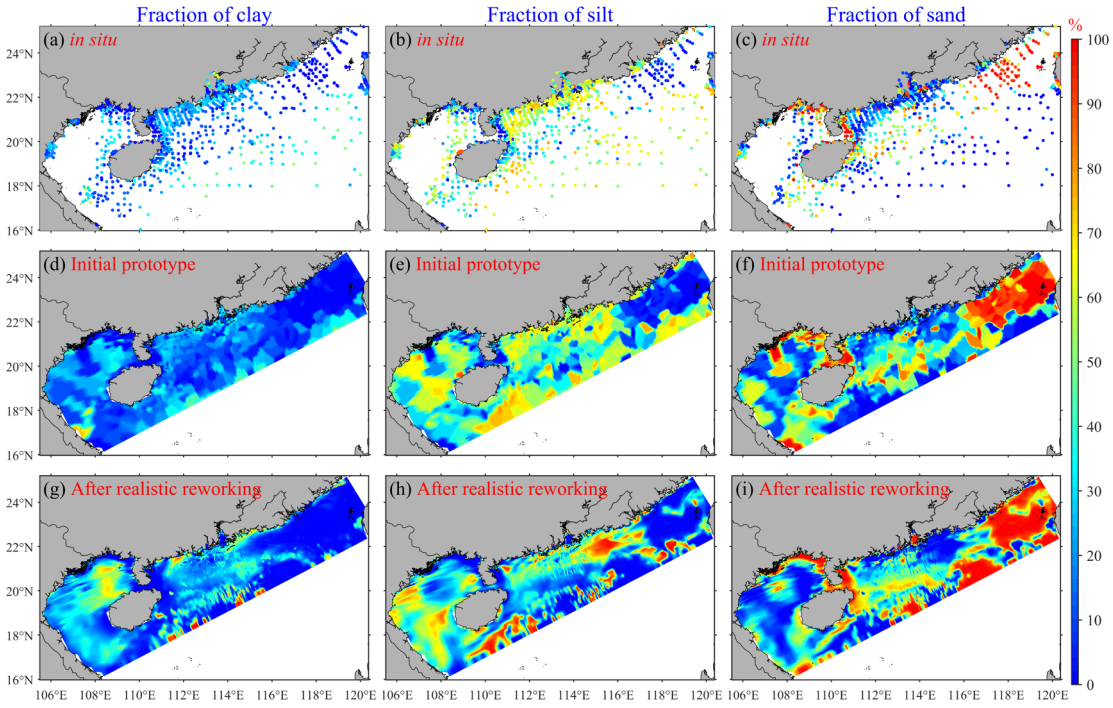

Figure 2. Row 1 presents the spatial distribution patterns of seabed sediment fractions derived from 1981 sampling sites, while Row 2 demonstrates the initial spatial distribution prototype of seabed sediment fractions developed based on the observational data presented in Row 1. Row 3 shows the spatial distribution patterns of seabed sediment fractions following the completion of spin-up phase in the Control run case on April 1st, 2017, with Columns 1, 2, and 3 representing the fractions of clay, silt, and sand, respectively.

As illustrated in Figure 2a-c, the measured stations exhibit a widespread distribution, offering comprehensive coverage of the entire northern continental shelf of the South China Sea, including the PRE. Particularly dense distribution is observed in the PRE and the coastal areas of western Guangdong. These regions represent the primary scope of transport and deposition associated with the Pearl River-derived sediment. Hence, the stations utilized in this study well represent the distribution of bed sediment particle size components in these study areas. It is evident that among the stations in the offshore area of the northern continental shelf of the South China Sea, silt dominates, followed by clay, while sand with the largest particle size is the least abundant. This suggests a significant presence of terrestrial sediment or Pearl River sediment in the offshore area of the northern continental shelf of the South China Sea. It should be noted that the lack of in situ grain size distribution data in specific regions of the model domain, especially in the Beibu Gulf area, may lead to uncertainties in sediment transport predictions. We will address these limitations and quantify their potential errors in the discussion part of this study.

To derive the component proportions of the initial prototype field on the model grid, this study employed the Kriging method (Krige, 1951), widely recognized for spatially interpolating various types of observational data. The sediment distribution pattern obtained through interpolation (Figure 2d-f) closely resembles the original 1981 measured sediment particle size distribution patterns (Figure 2a-c), suggesting the suitability of this interpolation method for the study area.

297 The initial prototype field underwent a 15-month spin-up period (from January 1,
298 2016, to March 31, 2017), during which it was adjusted by realistic reworking,
299 incorporating realistic hydrodynamics in ROMS, SWAN, and CSTM models. This
300 adjustment allowed for the redistribution of seabed sediment fractions based on the
301 modeled hydrodynamics. This method has been utilized in numerous previous studies,
302 including those by Bever et al. (2009), van der Wegen et al. (2010), and Zhang et al.
303 (2021). The realistic spin-up greatly reduced the irregularities and prepared a more
304 suitable seabed sediment particle size distribution field for subsequent simulations
305 than the initial prototype (Figures 2d-f vs. 2g-i).

306 During the 15-month spin-up and the subsequent 12-month formal model
307 simulations, the CSTM utilized five sediment classes (Table 1), which represent a
308 range of sediment sizes and characteristics, including three types of seabed sediments
309 (clay, silt, and sand, corresponding to the first three categories of sediments in Table 1)
310 and two types of Pearl River-derived sediments (the sum of the fourth and fifth
311 categories of sediments in Table 1, namely the riverine slow-settling single fine grains
312 (Class 4) and high-settling flocs (Class 5)). This approach allows for a better
313 distinction between Pearl River sediment and seabed sediment, enabling separate
314 analysis of the suspension, transport, and deposition of Pearl River-derived sediment
315 (Harris et al., 2008;Zhang et al., 2019). To clarify, the initial setup of the formal model
316 simulations excludes the retained riverine sediment (Class 4 and Class 5 in Table 1)
317 from the model domain during the spin-up period. The riverine flocs correspond to the
318 flocculated fractions of clay and silt, whereas the single fine grains represent the

non-flocculated components within the Pearl River-derived sediments, following the setting of Bever and MacWilliams (2013). Specifically, the fractions of the two types of Pearl River-derived sediments were set at 40% and 60%, respectively, following Zhang et al. (2019) and Zhang et al. (2021). The parameters for all five sediment classes are summarized in Table 1. Sediment density, porosity, and erosion rate for all sediment classes were set to 2650 kg m^{-3}, 0.672 (Zhang et al., 2019;Zhang et al., 2021), and 1×10^{-4} kg m^{-2} s^{-1} (Ralston et al., 2012), respectively. The settling velocity (w_s), critical shear stresses for erosion (τ_{ce}), and other parameters were set following previous studies or were based on model calibration (Ralston et al., 2012;Warner et al., 2017;Zhang et al., 2019;Dong et al., 2020;Zhang et al., 2021;Cao et al., 2025).

Our model configuration incorporates seasonal variations in τ_{ce}, supported by multiple lines of evidence from field observations, laboratory experiments, and numerical analyses (Dong et al., 2020;Cao et al., 2025). Previous studies have established a distinct seasonal pattern in the PRE, with winter τ_{ce} values significantly exceeding those in summer. Dong et al. (2020)'s laboratory experiments using the UMCES-Gust Erosion Microcosm System (U-GEMS) on 2017-winter sediment samples yielded a τ_{ce} of 0.26 Pa, which effectively reproduced observed SSC in winter simulations. However, this value proved excessive for summer conditions, where a τ_{ce} of 0.15 Pa provided better agreement with field observations in summer simulations, indicating a winter-to-summer τ_{ce} ratio of 1.73. Recent 2020-summer in situ measurements by Cao et al. using a benthic quadrapod-mounted 3D Profiling Sonar revealed a two-layer erosion threshold system: a surface "fluffy layer" with τ_{ce} = 0.06

Pa overlying a consolidated seabed with τ_{ce} = 0.13 Pa. The latter value aligns with Dong et al. (2020)'s summer calibration, suggesting that Dong et al. (2020)'s laboratory measurements, potentially affected by sediment consolidation during sample transport, might have missed the lower τ_{ce} of the surface fluffy layer. Based on these consistent findings, we implemented a seasonal τ_{ce} adjustment factor of 1.73 (winter/summer) in our model configuration (Table 1).

Table 1. CSTM model Sediment Properties

Source	Seabed			Pearl River	
Class	1	2	3	4	5
Sediment Type	Clay	Silt	Sand	single grains	flocs
w_s (mm s^{-1})	0.02[e]	1.2[c]	57[d]	0.005[e]	0.6[c]
Summer τ_{ce} (Pa)	0.14[cg]	0.03[c]	0.27[d]	0.15[abfg]	0.05[abcg]
Winter τ_{ce} (Pa)	0.24[cf]	0.05[cf]	0.47[df]	0.26[abf]	0.09[abcf]
Fraction	Spatially variable, see Figure 2g-i			40%[ab]	60%[ab]

[a]Zhang et al. (2019), [b]Zhang et al. (2021), [c]Ralston et al. (2012), [d]Warner et al. (2017), [e]Calibrated, [f](Dong et al., 2020), and [g]Cao et al. (2025).

2.5 Wet and dry season regimes

The study area exhibits pronounced seasonal variability, which can be distinctly categorized into two primary seasons (Dong et al., 2004;Su, 2004;Liu et al.,

2014;Zhang et al., 2021). This seasonal classification is supported by multiple environmental parameters, including river freshwater discharge, riverine sediment load (Figure 3a), wind patterns (Figure 3b), air temperature (Figure 3c), and modelled wave conditions (Figure 3d-f) at a representative site (21.5°N, 114°E; corresponding to station W1 in Figure S1a, located immediately south of the PRE). The meteorological data for wind and air temperature were obtained from the NCEP reanalysis dataset, while wave parameters were derived from numerical model simulations. These comprehensive indicators collectively characterize the distinct seasonal patterns observed in the study area (Figure 3). The entire year (from April 1, 2017, to March 31, 2018) is typically divided into two main seasons: wet summer (from April 1, 2017, to September 30, 2017) and dry winter (from October 1, 2017, to March 31, 2018).

During the wet summer season, freshwater discharge tends to be notably high, often exceeding 10,000 $m^3 s^{-1}$ and reaching a maximum of 53,000 $m^3 s^{-1}$, with an average value of 15,266 $m^3 s^{-1}$. This discharge constitutes a significant portion of the entire year, accounting for 72.06% of the annual total. During this period, the river carries a substantial sediment load of 32.85 megatons, constituting 95.17% of the total annual sediment transport. Prevailing winds predominantly blow from the south. For example, Figure 3b depicts the average monthly wind vector direction during the summer months as northward, with weak southeasterly winds in April, May, and September, and moderate southeasterly winds in July. June and August experience moderate southwesterly winds. The 2 m height air temperatures typically range

between 20℃ and 30℃. The daily average Hsig remains relatively low, with the monthly average Hsig less than 1 m. The wave propagation direction is generally consistent with the wind direction, being easterly in April and May, and southerly from June to September.

In stark contrast, the dry winter season demonstrates markedly lower runoff, typically falling below 10,000 $m^3 s^{-1}$, with an average value of 5,953 $m^3 s^{-1}$. The sediment load during this period is significantly reduced to merely 1.67 megatons, marking a substantial decrease compared to the wet summer season. Prevailing winds during the dry winter are predominantly northeasterly, with relatively high wind speeds. Except for moderate wind intensity in March, the monthly average wind speed in other months exceeds 5 m s^{-1}. The 2 m height air temperatures typically range between 10℃ and 25℃ during this season. The wave propagation direction aligns with the prevailing northeasterly winds of the season, predominantly northeasterly.

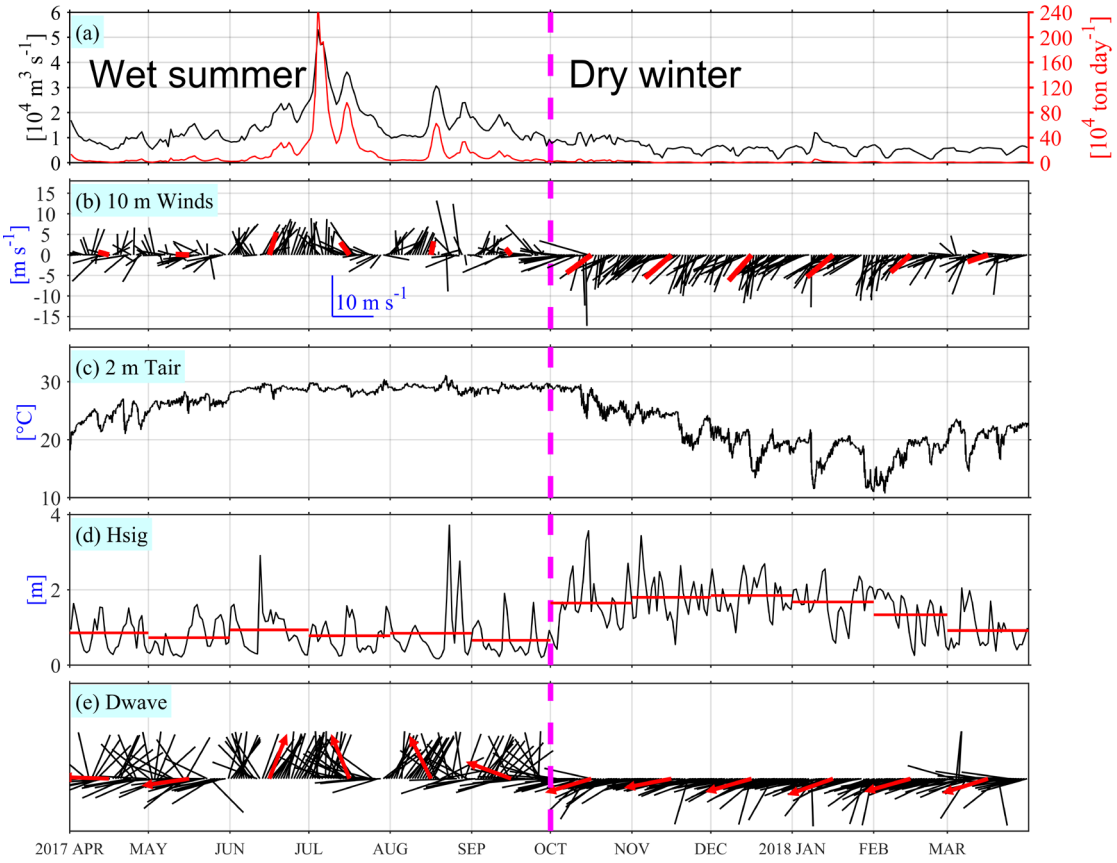

392

393 **Figure 3.** Time series of (a) the daily Pearl River freshwater discharge and sediment
394 load, (b) daily (black vectors) and monthly (red vectors) averaged 10-meter height
395 winds, (c) hourly 2-meter height air temperature, daily (black) and monthly (red)
396 averaged (d) significant wave height (Hsig, lines) and (f) wave propagation direction
397 (vectors) weighted by $Hsig^2$. Two distinct seasons are delineated by the dashed
398 magenta line.

399

400 ## 2.6 Model experiments

401 To assess the relative importance of tides, waves, ambient shelf currents and
402 residual water levels, seasonal variation in critical shear stress for erosion, the settling
403 velocity, and the sediment initial conditions in the transport and dispersal of Pearl

River-derived sediments, we conducted seven simulation experiments. Exp 1 (the ***Control*** run) incorporated all the aforementioned forcing agents (including winds) and accounted for the seasonal variation in critical shear stress for erosion, with the winter critical shear stress for erosion set to be 1.73 times of that in summer. Exp 2 (***NTS*** hereafter) was identical to Exp 1 but excluded tides, while Exp 3 (***NWS*** hereafter) excluded waves. In Exp 4 (***NAS*** hereafter), waves, tides, and the seasonal variation in critical shear stress for erosion were included, but the shelf current and residual water levels was omitted (i.e., no subtidal circulation forcing at open boundaries) to examine the influence of the South China Sea circulation. Then, Exp 5 (***NVS*** hereafter) was identical to Exp 1, except that it did not account for the seasonal variation in critical shear stress for erosion, keeping the winter and summer values the same. Exp 6 (***DSV*** hereafter) was identical to Exp 1, except that it set double sediment settling velocity of the Exp 1. Finally, to evaluate the model's sensitivity to sediment initial conditions, particularly focusing on the retention of riverine sediments within the water column and the seabed, we utilized the Control run's Class 1-5 sediment suspensions and depositions recorded on March 31, 2018, as alternative initial conditions for the five sediment classes. This configuration was implemented in the second control simulation, designated as Exp 7 (***Cycle*** hereafter). Consequently, this setup introduces a full year's worth of Pearl River-derived sediment suspensions and depositions into the model domain at the start of the ***Cycle*** experiment. In all experiments, we implemented the Charnock approach within COAWST's bulk air-sea flux parameterization scheme to calculate surface wind stress using the NCEP 10-m wind

product (Charnock, 1955;Fairall et al., 1996), ensuring consistency in wind stress forcing across all simulations.

3 Results

3.1 Seasonal hydrodynamics and Pearl River-derived sediment transport patterns

We quantified the spatial distributions of seasonal mean wind stress, Hsig, wave bottom orbital velocity (WBOV), and bottom shear stress for both the wet summer and dry winter periods (as defined in Section 2.5). These distributions serve as representative hydrodynamic conditions for typical summer and winter scenarios, respectively (Fig. 4).

During summer, the prevailing winds predominantly originate from south, with the average wind stress generally below 0.03 Pa, except in the eastern coastal waters of Hainan Island, where localized values reach up to 0.05 Pa (Fig. 4a). In contrast, during the dry winter season, the prevailing winds shift to a northeasterly direction, resulting in generally higher average wind stress compared to summer (Fig. 4b), with values typically exceeding 0.1 Pa in areas deeper than 40 m and surpassing 0.2 Pa in the offshore eastern Guangdong Coast near the Taiwan Bank.

Corresponding to the seasonal wind stress (Figures 4a-b), the seasonally averaged wave characteristics in the PRE and the adjacent northern continental shelf of the South China Sea exhibit significant seasonal variations (Figures 4c-d).

During the wet summer season, the Hsig in these areas is relatively low, with

448 waves predominantly coming from the southeast (Figure 4c). The seasonal average
449 Hsig across the entire shelf remains below 1 m, with areas deeper than 60 m showing
450 Hsig values above 0.8 m, while in shallower nearshore regions (water depth < 20 m),
451 Hsig is less than 0.6 m (Figure 4c). Corresponding to the lower Hsig in the wet
452 summer, the seasonally-averaged WBOV is also relatively small, generally less than 1
453 cm s^{-1} in areas deeper than 40 m, except in some nearshore shallow water regions
454 where it reaches up to 10 cm s^{-1} (Figure 4e). The seasonally-averaged bottom shear
455 stress during the wet summer is relatively high in the PRE, nearshore regions, and the
456 Taiwan Bank, where tidal dissipation is strong (Figure 4g).
457 In the dry winter season, the Hsig increases significantly compared to the wet
458 summer, with waves primarily coming from the northeast, although refraction occurs
459 in some nearshore regions, changing the wave direction to southeasterly (Figure 4d).
460 The area with water depths exceeding 60 m has a Hsig greater than 1.5 m, while in the
461 20-meter depth region, the Hsig reaches approximately 1 m (Figure 4d). Compared to
462 the wet summer, the WBOV increases significantly in the PRE mouth and many
463 nearshore regions, reaching up to 10-20 cm s^{-1} (Figure 4d). The average bottom shear
464 stress on the continental shelf outside the estuary also increases significantly during
465 the dry winter compared to the wet summer (Figure 4f).
466

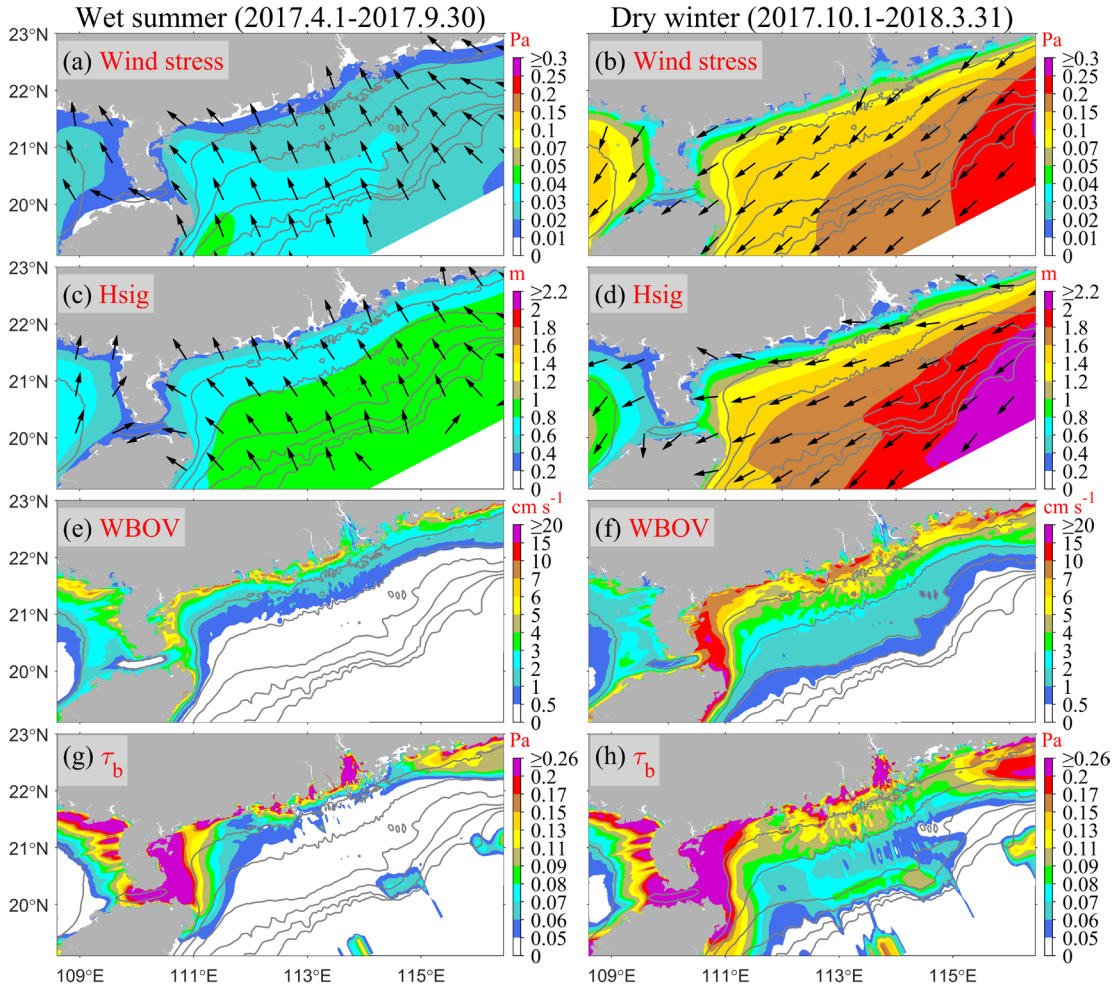

Figure 4. The patterns of variables averaged for the wet summer season (April 1st to September 30th, 2017; Column 1) and the dry winter season (October 1st to March 31st, 2018; Column 2) in the Control case. Row 1 (a-b) depicts wind stress (color) and direction (vectors), Row 2 (c-d) shows Hsig (color) and propagation direction (vectors) weighted by Hsig², Row 3 (e-f) presents wave bottom orbital velocity (WBOV), and Row 4 (g-h) displays bottom shear stress magnitude.

The patterns of residual sediment dispersal, flux, and deposition over the simulation period provide clear information on the mechanisms for sediment redistribution on both annual and seasonal timescales. This section presents a detailed

analysis of the seasonally averaged fields of salinity, flow, riverine SSC, depth-integrated riverine sediment flux, and riverine sediment deposition patterns during the wet summer season (Figure 5) and dry winter season (Figure 6) on the continental shelf.

During the wet summer season, the Pearl River discharges a significant amount of freshwater and sediment (Figure 3a), resulting in an extensive expansion of the river plume into the sea, primarily in the surface layer (Figure 5a-b). The river plume extends both eastward and westward along the coastline (Figure 5a). Due to the influence of southerly winds (Figure 4a) and ambient shelf currents, the extent of the river plume extending eastward is significantly higher than that extending westward.

In terms of riverine sediment suspension, its maximum turbidity zone (~100 mg L^{-1}) is situated in the shallow water area within the estuary (water depth < 10 m). Beyond the estuary, suspended riverine sediment disperses across the shelf through the river plume. Further away from the estuary, its distribution aligns with that of the river plume, with concentrations diminishing as dispersal distance increases. Integrating the horizontal flux of riverine sediment vertically offers a clear indication of the primary transport pathway of riverine sediment (Figure 5e). The riverine sediment exhibits both westward and eastward fluxes (Figure 5e). Westward coastal transport can extend as far as the Leizhou Peninsula and Hainan Island. On the eastern side, the eastward transport extends toward the Taiwan Bank. However, the primary transport pathway is diverted southward (Figure 5e) due to the obstruction caused by summer upwelling near the Guangdong east coast (Chen et al., 2017a;Chen et al.,

2017b), as evidenced by the cross-shore current in the bottom layer (Figure 5b). The westward transport pathway follows the region where the water depth is shallower than 30 m, with a riverine sediment flux of 10–20 g^{-1} m s^{-1}. In contrast, the eastward transport pathway occurs in the 30–60 m depth range, but the riverine sediment flux is below 10 g^{-1} m s^{-1}. Throughout the wet summer season, substantial amounts of riverine sediment are deposited near the estuary (Figure 5d), particularly leading to notably high deposition of riverine sediment near the river mouth (> 100 mm). Outside the estuary, the thickness of riverine sediment is comparatively lower, but it can reach approximately ~0.5 mm during the wet summer season in certain areas off the coast of western Guangdong.

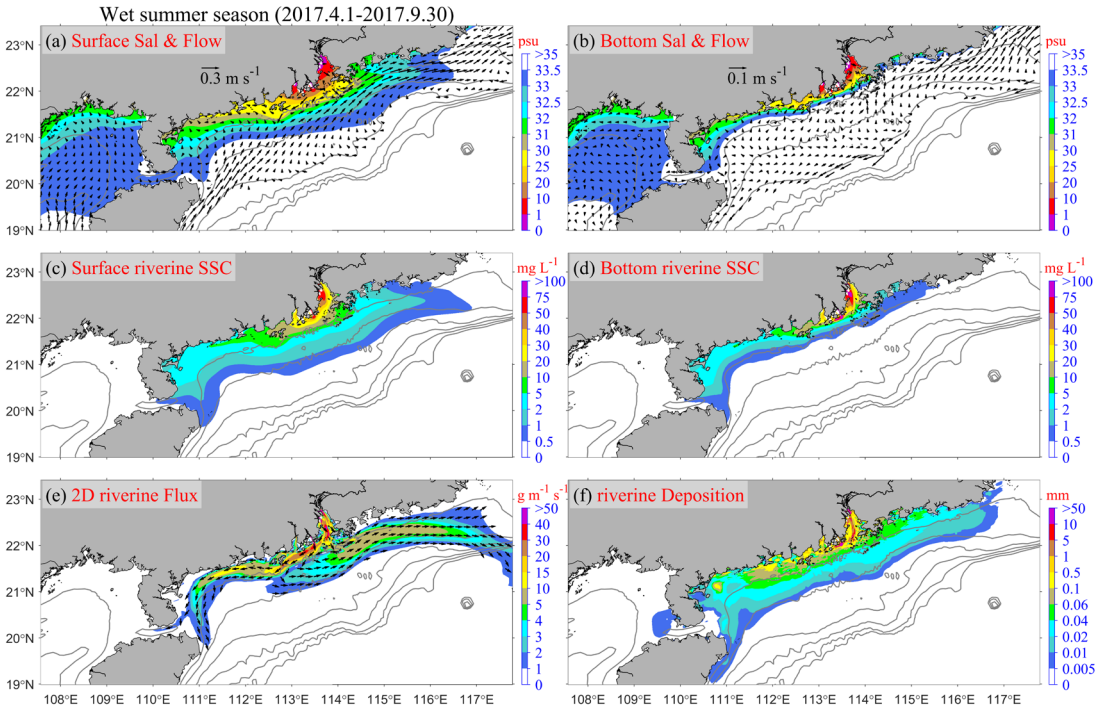

Figure 5. Patterns averaged over the entire wet summer season in the Control case: (a) surface and (b) bottom salinity (color, psu) and flow (arrows, m s^{-1}); (c) surface and (d)

514 bottom riverine SSC (mg L^{-1}); (e) depth-integrated riverine sediment transport rate
515 (color, g m^{-1} s^{-1}) and direction (arrows); and (f) riverine deposition thickness during
516 the wet summer season (mm). Flow vectors in regions with water depths exceeding
517 100 m are masked for clarity.
518
519 During the dry winter season, runoff from the Pearl River significantly decreases
520 compared to the wet summer (as indicated in Figure 3a), accompanied by strong
521 northeasterly winds (Figure 4b). Consequently, the expansion of the Pearl River
522 plume is constrained to the westward direction only, resulting in a narrow cross-shore
523 width of the plume and the formation of a strong horizontal salinity gradient outside
524 the estuary (Figure 6a). Flow velocity is increased near the salinity front, allowing
525 river plume to extend westward through the Qiongzhou Strait to the Beibu Gulf. With
526 sediment load during winter nearly negligible, the suspended concentration of riverine
527 sediment is significantly lower compared to the wet summer (Figure 6b). In areas
528 beyond the estuary, it is typically less than 3 mg L^{-1}, whereas inside the estuary, it is
529 around ~5 mg L^{-1}. During the dry winter, following the transport path of river plume,
530 riverine suspended sediment primarily moves westward along the coast, deflecting
531 southward along the topography near the Leizhou Peninsula (Figure 6c). It then
532 bifurcates near the east entrance of the Qiongzhou Strait, with one branch continuing
533 into the Beibu Gulf, and the other branch proceeding southward along the east coast
534 of Hainan Island. Stronger winds and waves in the dry winter lead to the resuspension
535 of a considerable amount of riverine sediments, originally deposited in estuaries and

shelf seas during summer. The resuspended sediments are then transported to coastal bays as well as to the sides and rear of the islands (Figure 6d). Additionally, a portion of the riverine sediment transported to the Beibu Gulf gets deposited on the seabed during the dry winter season.

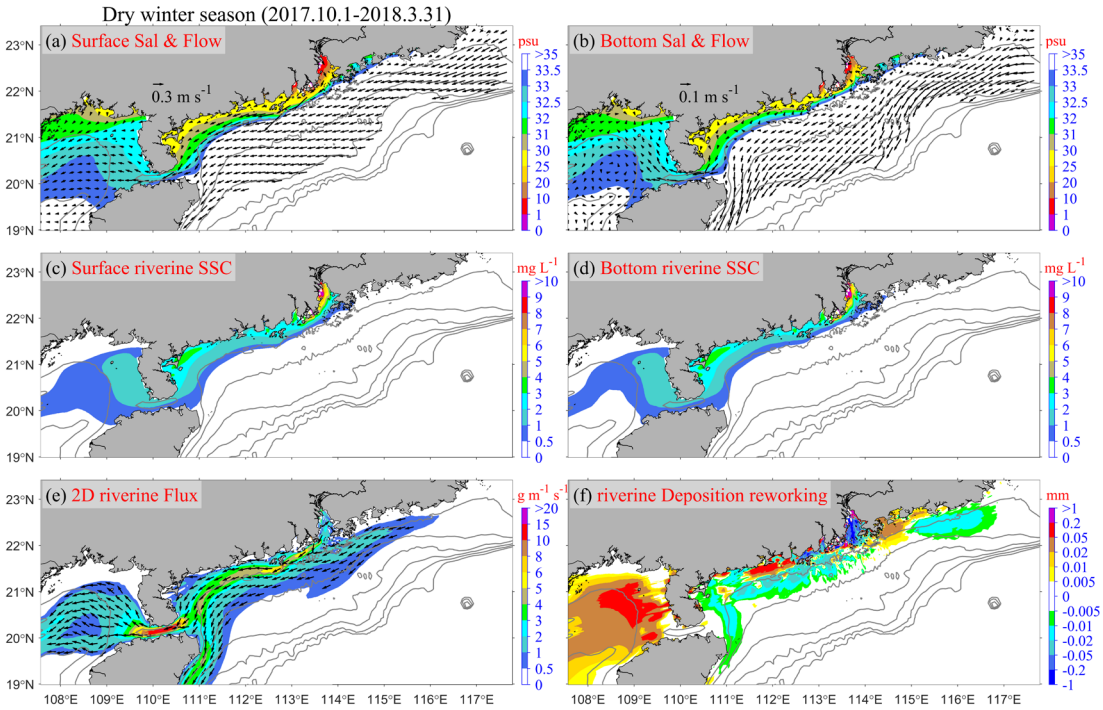

Figure 6. Same as Figure 5, but for the dry winter season in the Control case. Notably, (f) illustrates the changes in riverine sediment deposition on the seabed at the end of the dry winter season compared to the end of the wet summer season.

3.2 Riverine sediment budgets and annual deposition over the shelf

To improve the understanding of the spatial-temporal variabilities in the riverine sediment dispersal, and the estimation of the fate of the Pearl River sediment during the wet summer season, dry winter season, and throughout the year, we partitioned the

model domain into eight distinct regions delineated by various transects as illustrated in Figure 1. The division criteria are mainly based on the distance from the estuary and the natural separation by the Leizhou Peninsula and Hainan Island. These areas include:

① Proximal region: Proximity to the estuary,

② Southern region: Located deeper in the southern part of the estuary,

③ Eastern region: Eastern side of the estuary, closer to the shoreline,

④ Southeastern region: Further offshore on the eastern side of the estuary,

⑤ Western region: Western side of the estuary, closer to the shoreline,

⑥ Southwestern region: Offshore on the western side of the estuary,

⑦ Gulf region: Mainly the Beibu Gulf,

⑧ Distal region: South of the Hainan Island.

By dividing the model domain into these delineated regions, we calculated the riverine sediment flux for each transect, thereby determining the total riverine sediment volume retained in each region. Additionally, Figure 7a-c illustrates the proportion of riverine sediment retention budget within each region, expressed as a percentage of the total annual river sediment input, for the wet summer season, the dry winter season, and the entire year under the Control run case, respectively. Meanwhile, Figure 7d illustrates the annual deposition over the shelf.

The retention of Pearl River sediment on the continental shelf exhibits significant seasonal variations (Figure 7a-c). During summer (characterized by high discharge and low wind/waves), the PRE and continental shelf receive 95.17% of the annual

572 sediment load from the Pearl River (Figures 3a and 7a). Approximately two-thirds of
573 this sediment is retained in the "Proximal" region (Figure 7a). Additionally, influenced
574 by the prevailing southerly winds and northeastward background circulation, 13.01%
575 of the annual sediment load is retained on the shelf east of the PRE, specifically in the
576 "Eastern" and "Southeastern" regions. Meanwhile, the shelf west of the PRE retains
577 15.87% of the annual load, with the "Western" region being the primary receiver,
578 accounting for 8.48%. Only 0.92% and 2.3% of the annual load enter the "Gulf" and
579 "Distal" regions, respectively, during summer. The "Southern" region retains a mere
580 1.33% of the sediment. In winter (characterized by low discharge and energetic
581 winds/waves), the PRE and continental shelf receive only 4.83% of the annual
582 sediment load (Figures 3a and 7b). The sediment distribution during this season is
583 primarily a result of the dynamic reworking of the sediments of summer deposition
584 (Figure 7b). While the "Proximal" region continues to receive sediment, with a 1.38%
585 increase in retention, the other five regions east of the Leizhou Peninsula and Hainan
586 Island experience a decrease in sediment retention. This sediment is predominantly
587 transported and retained to the more distant "Gulf" and "Distal" regions. The annual
588 sediment budget reveals that 66.45% of the Pearl River sediment is retained in the
589 "Proximal" region. Additionally, 9.2% is retained on the shelf east of the estuary,
590 primarily during summer, while 24.12% is retained on the shelf west of the estuary,
591 with the majority deposited in the distal regions of the Beibu Gulf and south of
592 Hainan Island, mainly during winter.

593 The annual deposition thickness of Pearl River sediments, as illustrated in Figure

7d, reveals significant proximal deposition within and near the estuary, with many areas exceeding 10 mm despite winter resuspension and transport. Additionally, deposition on the inner shelf (water depth <60 m) to the east of the PRE reached a magnitude of 0.1 mm, while the western shelf of the PRE exhibited significantly greater accumulation. For instance, the deposition west of the Chuanshan Islands reached a magnitude of 0.5 mm. In the Beibu Gulf region, deposition was primarily concentrated in the northeastern part of the gulf, extending southwestward along the 30-60 m isobaths. Sediments transported southwestward along the eastern coast of Hainan Island and retained in the "Distal" regions did not predominantly settle on the seabed due to the greater water depth but remained largely suspended in the water column.

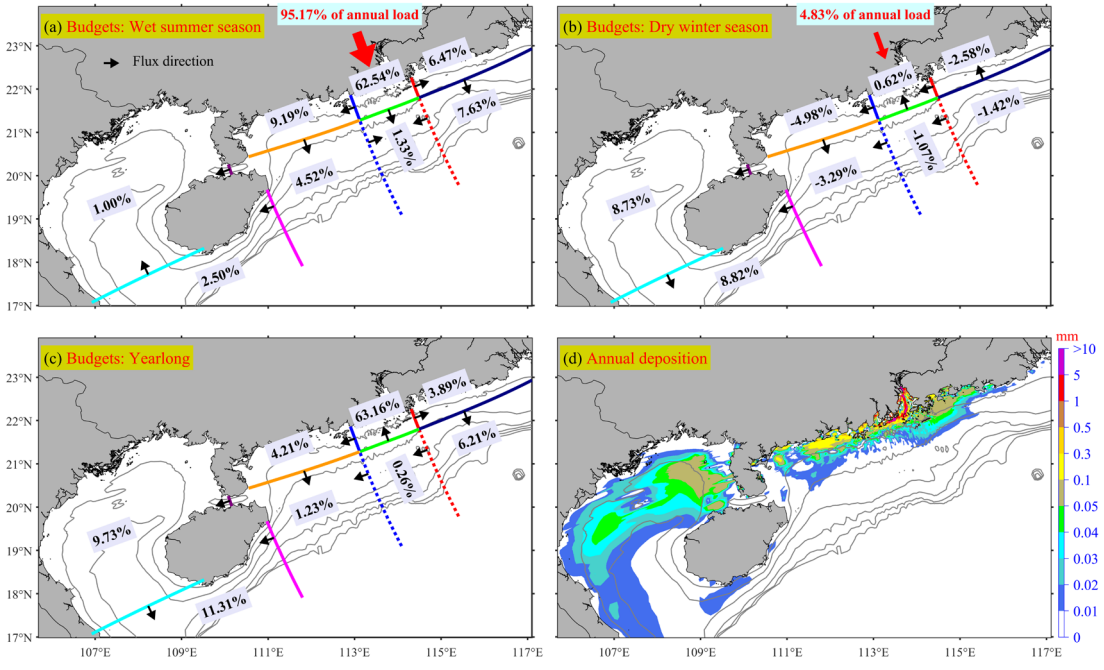

Figure 7. Riverine sediment retention budget percentages at eight regions during (a) the wet summer season, (b) the dry winter season, and (c) the entire year in the Control run case. (d) Same as Figure 5d, but shows the annual deposition patterns spanning from April 1st, 2017, to March 31st, 2018 in the Control Run. All percentages displayed in the figure are relative to the annual riverine sediment load. The black percentage values represent the combined total of riverine sediment Class 4 and Class 5, while the red and blue values denote sediment Class 4 and Class 5, respectively. Arrows indicate the direction of net riverine sediment flux at each transect during the specified period.

3.3 Model sensitivity experiments: relative roles of physical processes, sediment properties, and initial conditions

Six sensitivity simulations, namely Exp 2-7 (NTS, NWS, NAS, NVS, DSV, and Cycle), were conducted. As the latter three experiments do not impact hydrodynamics, we focus on presenting the seasonal mean differences in bottom shear stress between the Control run and the first three cases (NTS-Control, NWS-Control, NAS-Control) for both summer and winter (Figure 8).

Tidal and wave forces significantly influence bottom stress. In the NTS case, where tidal forces were excluded, the underestimation of bottom shear stress was similar in both summer and winter due to the minimal seasonal variation in tidal intensity. This underestimation primarily occurred in the PRE, around the Taiwan Bank, and near the Leizhou Peninsula (Figure 8a-b). In contrast, the NWS case, which

629 excluded wave forces, showed a greater underestimation in winter than in summer,
630 reflecting the intense seasonal variability of wind and wave activities (Figure 3b, 3d-e,
631 and 4a-f). Unlike the NTS case, the NWS case mainly underestimated the bottom
632 stress in the nearshore areas outside the PRE, though it similarly underestimated the
633 bottom stress around the Taiwan Bank and the eastern side of the Leizhou Peninsula
634 (Figure 8c-d). For the NAS case, where ambient shelf currents and residual water
635 levels at the model boundaries were excluded, the impact on bottom stress was
636 minimal compared to the NTS and NWS cases. The effect was almost negligible on
637 the inner shelf at depths less than 100 m, with widespread impacts generally below
638 0.02 Pa. Some overestimations were noted in localized deeper areas near the
639 boundaries, probably being artifacts, but these changes in bottom stress, being distant
640 from the Pearl River sediment distribution areas, did not affect the dynamics of the
641 Pearl River sediment (Figure 8e-f).
642

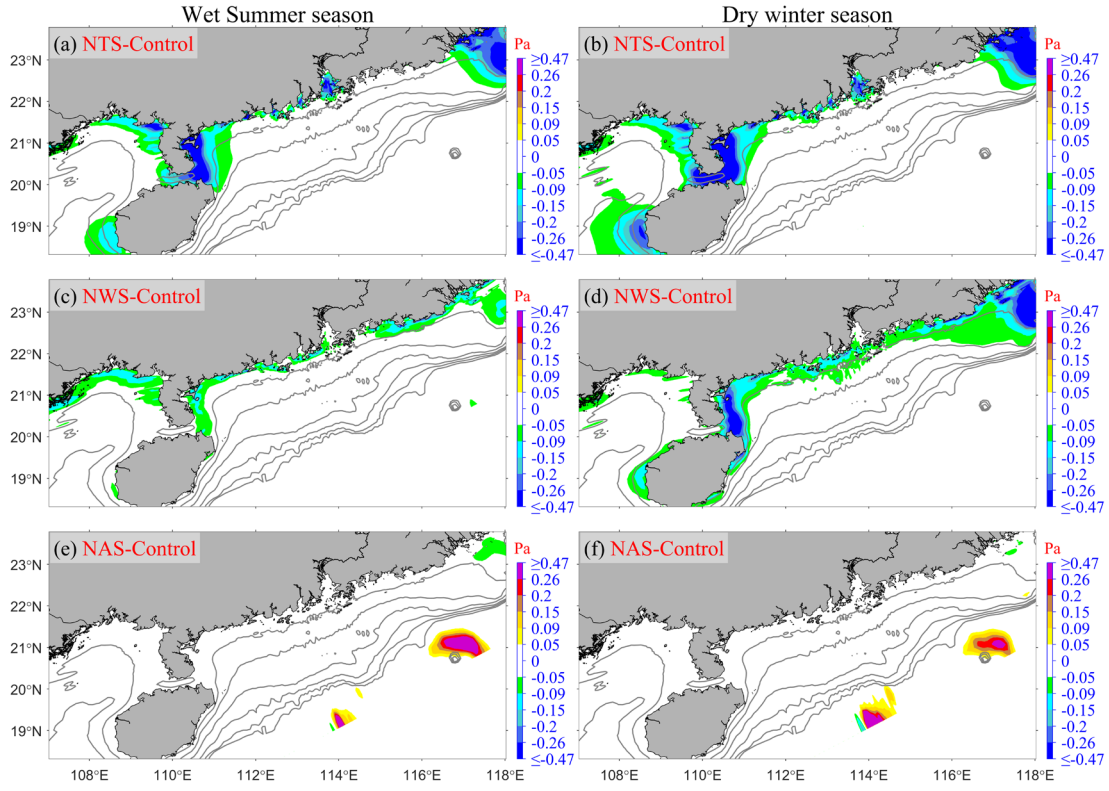

643

644 **Figure 8.** The seasonal mean differences in bottom shear stress between the Control
645 run and the following cases: (a-b) NTS (NTS minus Control), (c-d) NWS (NWS
646 minus Control), and (e-f) NAS (NAS minus Control). The first column represents the
647 wet summer season, while the second column corresponds to the dry winter season.

648

649 Following the bottom shear stress analysis (Figure 8), we analyzed seasonal
650 sediment transport and deposition patterns by comparing the control run with six
651 sensitivity experiments (NTS-Control, NWS-Control, NAS-Control, NVS-Control,
652 DSV-Control, and Cycle-Control) (Figures 9-11). The study focuses on Pearl
653 River-derived sediment dynamics, indicated by surface circulation and SSC
654 distribution patterns (Figures 5 and 6). Specifically, Figures 9 and 10 present seasonal
655 surface currents and SSC differences between control and sensitivity runs,

complemented by deposition pattern differences in Figure 11.

For the NTS case versus the Control case, tides significantly affected bottom stress (Figures 8a-b) but had minimal impact on the mean circulation (Figures 5a, 6a, and 9a-b). The exclusion of tides substantially reduced bottom shear stress in the PRE and near the Leizhou Peninsula, weakening sediment resuspension. Consequently, increased deposition of Pearl River-derived sediments occurred in the PRE, its adjacent areas, and on both sides of the Leizhou Peninsula (Figure 11a). During summer, riverine SSC notably decreased in the PRE and the inner shelf east of the Leizhou Peninsula (Figure 9a). This reduction pattern persisted in winter, particularly in the PRE and on both sides of the Leizhou Peninsula (Figure 9b).

In the NWS case with waves excluded, like the NTS, NWS had a relatively minor impact on circulation (Figures 5a, 6a, and 9c-d). However, NWS underestimated the nearshore bottom stress (Figures 8c-d). This led to more Pearl River-derived sediment being deposited outside the PRE and in the nearshore shallow waters along the Guangdong Coastline (regions significantly affected by waves) (Figure 11b). Consequently, the riverine SSC in summer was much lower in the downstream of the PRE and on the inner shelf east of the Leizhou Peninsula (Figure 9c). This similar reduction pattern persisted in the winter, but is slightly in more western regions (Figure 9d).

For the NAS case in which ambient shelf currents and residual water levels at the model boundaries were excluded, the impact on bottom stress was minimal compared to the NTS and NWS cases. However, NAS had a relatively large impact on the mean

678 circulation (Figures 5a, 6a, and 9e-f). It mainly influenced the summer circulation.
679 Specifically, ignoring these factors would cause the relatively strong northeastward
680 flow along the Guangdong coast to become very weak (Figure 9e). When it comes to
681 winter, the influence of NAS on circulation was relatively small. That is, in the
682 absence of the background residual water level and residual current, due to the strong
683 northeastward winds in winter, the overall circulation was still southwestward (Figure
684 9f). The underestimated northeastward flow in summer led to the Riverine SSC being
685 scarcely transported to the vicinity of the Eastern Guangdong Coastline. Consequently,
686 the Riverine SSC there was decreased (Figure 9e) and sediment deposition was
687 significantly reduced (Figure 11c). Most of the suspended Riverine sediment was
688 transported southwestward, resulting in an increase in the Riverine SSC along the
689 Western Guangdong Coastline. In winter, since most of the suspended Riverine
690 sediment had been transported southwestward in summer, the Riverine SSC decreased
691 compared to the Control run (Figure 9f). Ultimately, NAS mainly caused a significant
692 reduction in sediment deposition near the Eastern Guangdong Coastline, while
693 sediment deposition increased in the Beibu Gulf and the "Distal" region (Figure 11c).

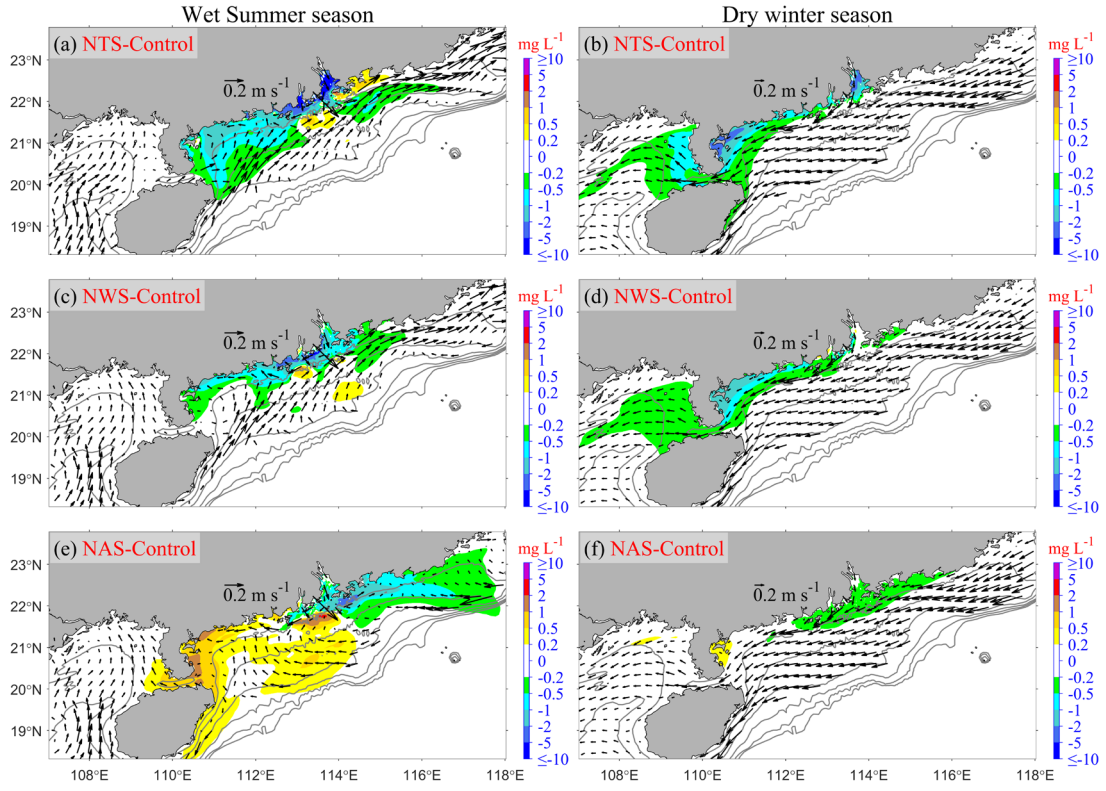

694

695 **Figure 9.** Same as Figure 8, but for seasonal mean differences in surface SSC
696 between the Control run and the following cases: (a-b) NTS-Control, (c-d)
697 NWS-Control, and (e-f) NAS-Control. The first column represents the wet summer
698 season, while the second column corresponds to the dry winter season. Vectors show
699 the seasonal mean surface current fields in each experiment.

700

701 For the NVS case, in which the winter and summer critical shear stress for
702 erosion were kept identical, the summer conditions of NVS were precisely the same
703 as those of the Control run (Figure 10a). Since the critical shear stress for erosion in
704 winter was lower than that in the Control run, this led to an increase in re-suspension
705 within the PRE, along the Western Guangdong Coastline, and in the Beibu Gulf area,
706 resulting in an increase in Riverine SSC (Figure 10b). Eventually, this caused a

reduction in the deposition thickness of Pearl River-derived sediments on the continental shelf (Figure 11d).

In the DSV case, where sediment settling velocity was doubled compared to the Control run, riverine SSC patterns remained broadly similar between the two scenarios in both summer and winter. However, significant reductions occurred in the primarialy high SSC areas, with regions of higher SSC in the Control run experiencing the most pronounced declines (Figures 5c, 6c, 10c-d). This enhanced settling velocity resulted in an increased deposition of Pearl River-derived sediments along the Guangdong coastline and the eastern Beibu Gulf, accompanied by a reduced deposition thickness in the western Beibu Gulf (Figure 11e).

In the Cycle case, the initial conditions for the five sediment classes were set using the Class 1-5 sediment suspensions and depositions from the Control run on March 31, 2018, initiating a second control simulation. This setup introduced a full year's result of Pearl River-derived sediment suspensions and depositions into the model domain at the start. Consequently, during the initial summer period, the Cycle case elevated riverine SSC in the primary depocenters identified in the Control run (Figures 7d and 10e), while this effect diminished by winter (Figure 10f). This experiment specifically examines the impact of pre-existing Pearl River-derived sediments in the water column and seabed on annual seabed budgets. To isolate this effect, the sediment thickness from the Control run's end on March 31, 2018, was subtracted as a baseline before comparing annual depositions with the Control run (Figure 11f). The Cycle case changed the downstream PRE deposition patterns, with

729 increased sediment accumulation in downstream regions and notable changes in
730 deposition thickness in parts of the Beibu Gulf, revealing a long-term southwestward
731 sediment transport trend.

732

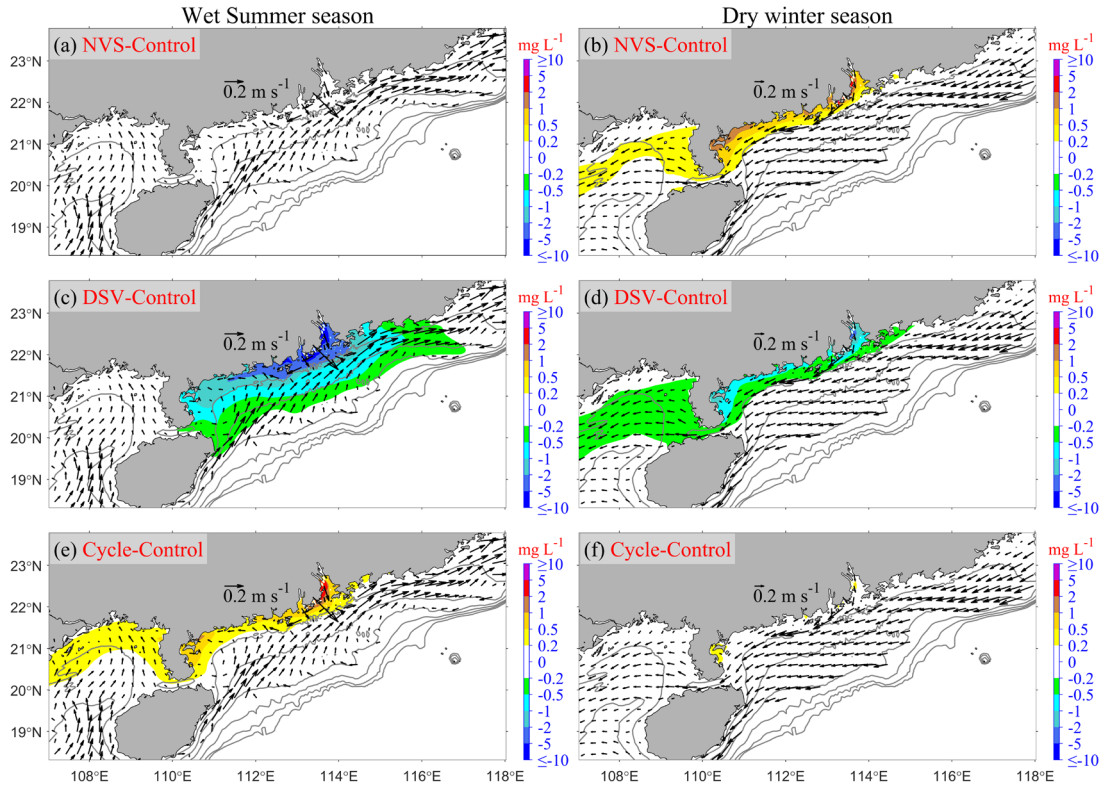

733

734 **Figure 10.** Same as Figure 9, but for the latter three experiments (NVS, DSV, Cycle).
735 (a-b) NVS-Control, (c-d) DSV-Control, and (e-f) Cycle-Control.

736

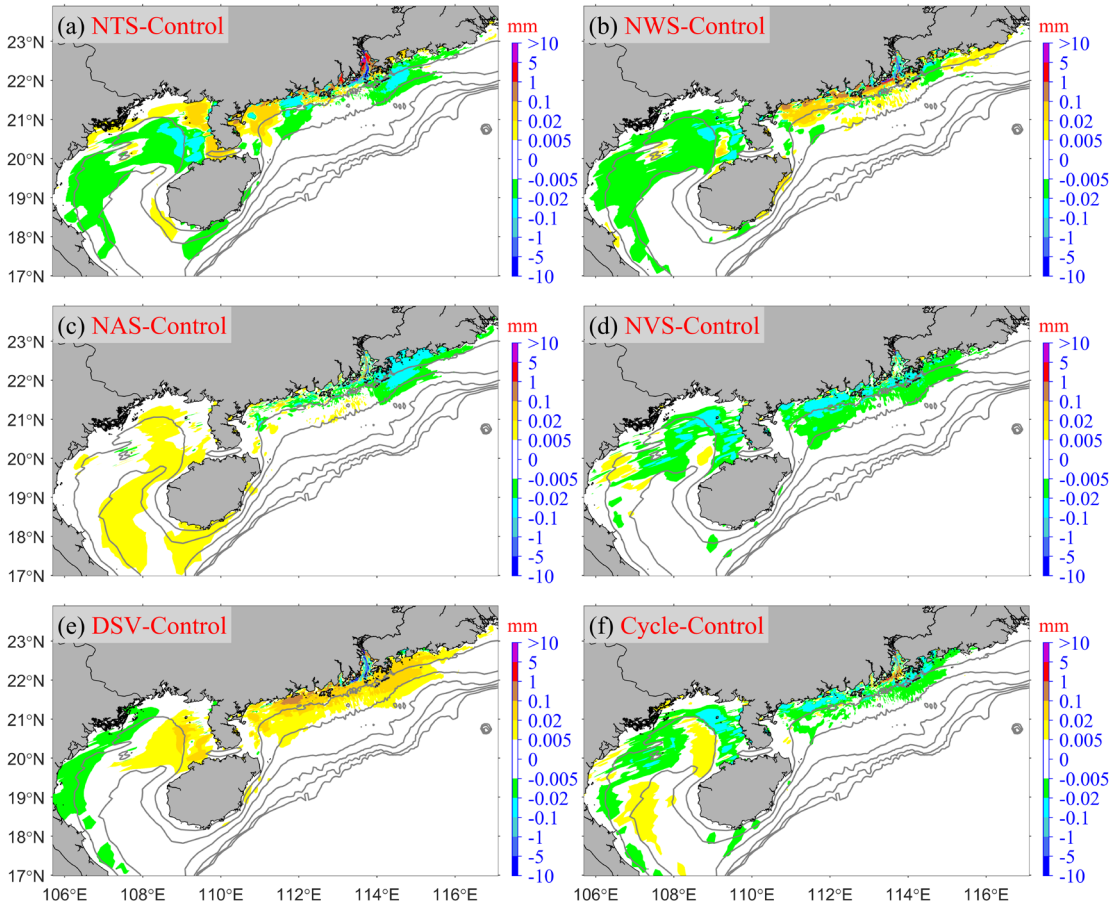

737

738 **Figure 11.** The differences in annual deposition between the Control run and the

739 following cases: (a) NTS-Control, (b) NWS-Control, (c) NAS-Control, (d)

740 NVS-Control, (e) DSV-Control, and (f) Cycle-Control.

741

742 Finally, we analyze the impact of various factors on the annual riverine sediment

743 retention budget across different regions. Specifically, Figure 12 illustrates the annual

744 riverine sediment retention budget in various regions under six sensitivity simulations,

745 namely Exp 2-7 (including NTS, NWS, NAS, NVS, DSV, and Cycle). It should be

746 noted that the retention percentages budget and their variations discussed hereinafter

747 are all relative to the annual riverine sediment load.

As shown in Figure 12, tides and sediment settling velocity have the most significant impact on the retention in the "Proximal" region. In the NTS case and the DSV case, the retention in the "Proximal" region is 70.92% and 71.57%, respectively (Figures 12a and 12e), which is higher than 66.45% in the Control run (Figure 7c). This indicates that ignoring tides will cause the PRE to capture more riverine sediments, and a larger settling velocity will result in more riverine sediments being retained within the PRE. In these two cases, compared with the Control run, the retention in the "Gulf" and "Distal" regions decreases. Meanwhile, the DSV case causes the greatest increase in retention in the "Western" region, with an increase of +1.91%.

Furthermore, the NWS also leads to a 2.2% increase in retention in the "Proximal" region (Figure 12b), which is lower than that in the NTS case. This shows that tides dominate resuspension versus deposition in the estuary more than waves do. However, for the "Western" region on the shelf west of the PRE, compared with the NTS case, the NWS causes a greater increase in retention, indicating that waves dominate the resuspension of Pearl River-derived sediments in these nearshore areas more than tides do.

For the shelf east of the PRE (i.e., the "Eastern" and "Southeastern" regions), NAS brings about the most dramatic changes. In the absence of ambient shelf currents and residual water levels, the retention of Pearl River-derived sediments in these regions drops from 9.1% to 0.84% (Figure 12c). Meanwhile, ignoring these background circulations results in a substantial overestimation of the retention in the

"Distal" region, with an increase of 6.49%.

In the NVS case, where the winter and summer critical shear stress for erosion are set to be identical, ignoring the fact that the critical erosion stress in winter should be higher than that in summer leads to a decrease in the retention of Pearl River-derived sediments on the shelf east of the Leizhou Peninsula and Hainan Island. The reduction ranges from -0.05% to -0.85% (Figure 12d), which in turn causes the retention in the "Gulf" and "Distal" regions to increase by 0.7% and 1.47%, respectively. Overall, compared with scenarios that ignore physical processes and alter sediment settling velocity (NTS, NWS, NAS, and DSV), the NVS scenario, which does not take into account the seasonal variation of critical shear stress for erosion, has a relatively smaller impact on the retention of Pearl River-derived sediments.

Finally, in the Cycle case, the end state of the Control run is used as the initial conditions, and a second control simulation is performed. To isolate the pre-existing Pearl River-derived sediments, the initial retentions (the end conditions of the Control run on March 31, 2018) are subtracted before calculating the retention in the Cycle case (Figure 12f). In the Cycle case, the retention of Pearl River-derived sediments on the shelf east of the Leizhou Peninsula and Hainan Island shows little variation, with values ranging from -0.98% to +0.24% (Figure 12f). The most significant changes are the decreases and increases in retention in the "Gulf" and "Distal" regions, which are -2.17% and +3.54%, respectively, compared to the Control run. This demonstrates the long-term trend of southwestward transport of Pearl River-derived sediments on the shelf (relative to the Control run).

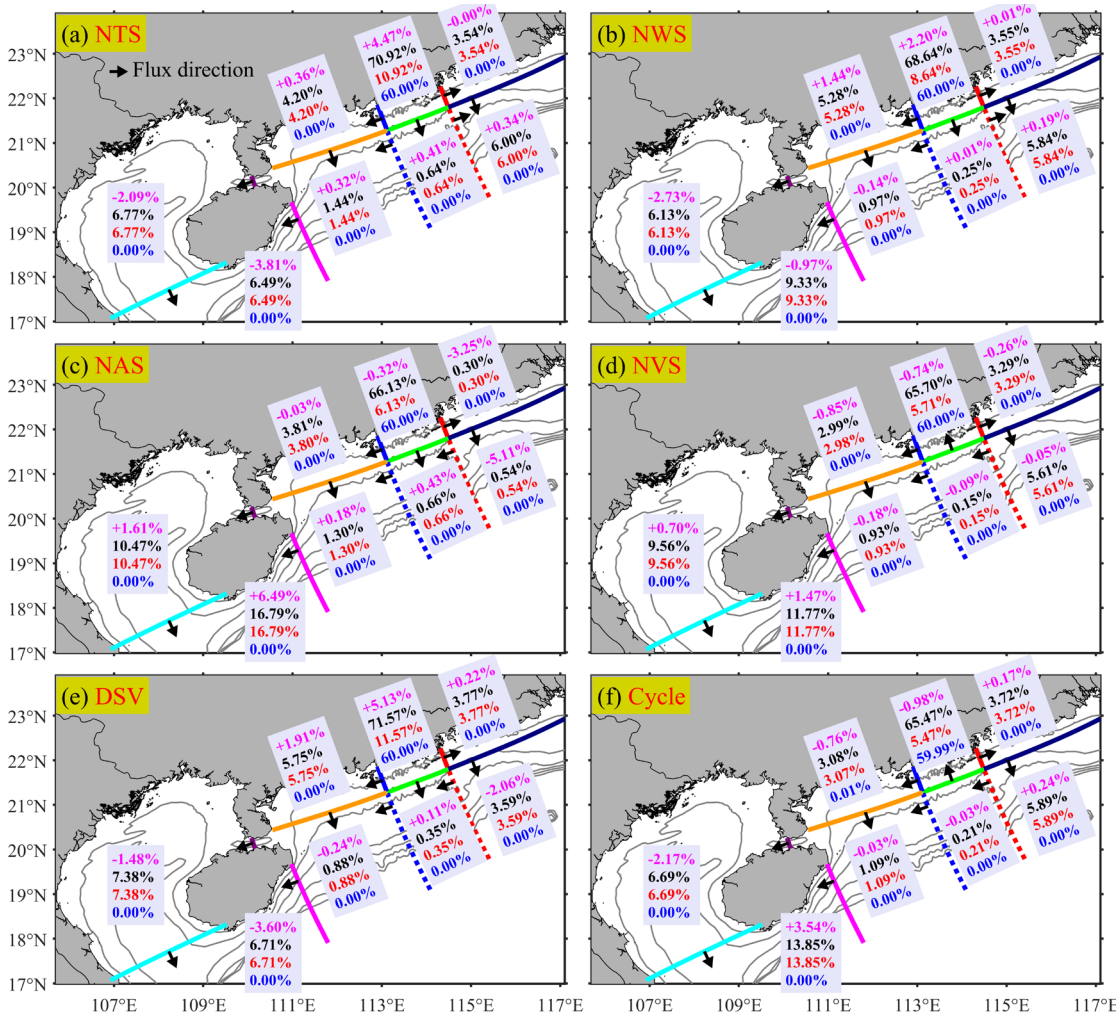

Figure 12. Same as Figure 7c, but for the other six cases: (a) NTS, (b) NWS, (c) NAS, (d) NVS, (e) DSV, and (f) Cycle, respectively. The magenta percentage values indicate the retention percentage budget differences between the Control run and the sensitivity cases.

4. Discussions

4.1 Fidelity of our model results

We simulated the suspension, transport, and deposition of Pearl River-derived sediment over the shelf from April 2017 to March 2018. Comparisons with multiple types of observations demonstrated that the model simulation reasonably well captured the regional patterns and temporal variability of water levels (Figures S2-S4), surface waves (Figures S5-S6), estuarine and shelf currents (Figures S8a-b and S9-S10), salinity and temperature (Figures S7a-b and S8c-d), and SSC (Figures S7c and S8e-f). Even though we have made substantial efforts to collect observational data and conduct calibration and validation, the large scope of the study area and the fact that the study covers an entire year mean that there are some inherent challenges to achieving a complete analysis. The real-world situation may be extremely complex, and these validations may still not be sufficient to address all issues (such as the accurate parameterization of sediment characteristics and their seasonal variations, as well as the proportion of slow-settling fine grains and flocculated materials in riverine sediments). Therefore, in this section, we intend to discuss the fidelity of our results.

Firstly, according to previous observations, laboratory experiments, and numerical sensitivity analyses, it has been demonstrated that the critical shear stress for erosion of sediments in the PRE is higher in winter than in summer (Dong et al., 2020;Cao et al., 2025). Therefore, we considered the seasonal variation of critical shear stress for erosion in a suite of model experiments, that is, increasing the critical shear stress for erosion in winter. This setting was also applied during the 15-month

822 spin-up before conducting the model experiments (the driving force of the spin-up is
823 realistic, i.e., the settings are consistent with those of the Control run). After realistic
824 reworking during the spin-up, the bed sediment grain size distribution (used as initial
825 conditions in the Control run and all Sensitivity cases except the Cycle case) is quite
826 close to the initial prototype (Figures 2d-f vs. 2g-i) compared to our previous spin-up
827 (not presented in this version; however, it can be referred to in our initially submitted
828 preprint and Supplement), which did not consider such temporal variability.

829 When the seasonal variation of critical shear stress for erosion is not considered,
830 the results of the NVS case indicate that such a setting underestimates the retention of
831 Pearl River-derived sediments on the shelf east of the Leizhou Peninsula and Hainan
832 Island during winter, while overestimating the retention in the "Gulf" and "Distal"
833 regions. Even so, these estimation errors are relatively minor compared to the annual
834 load (Figure 12d). Consequently, the consideration of the seasonal variation of critical
835 shear stress for erosion has a relatively small impact on the annual retention. Instead,
836 it has a more significant effect on the bed sediment grain size distribution at the
837 bottom.

838 Furthermore, although the initial bed sediment grain size distribution we obtained
839 by considering the seasonal variation of critical shear stress for erosion is quite close
840 to the initial prototype, there are still some differences (Figures 2d-f vs. 2g-i).
841 Additionally, the lack of in situ grain size distributions in part of the model domain
842 (especially in the Beibu Gulf) may also introduce some uncertainties in sediment
843 transport there. Does the variation in the proportion of bed sediment grain sizes have a

844 significant impact on the model results? It should be noted that here we are not
845 referring to the distribution proportion of riverine sediments on the bed. To address
846 this question, we designed a new experiment (Cycle2). We used the end state of the
847 Control run on March 31, 2018, as the initial conditions for Cycle2. However,
848 different from the Cycle case, in Cycle2, we changed both Class 1 and Class 4
849 sediments in the bed and water column at the end state of the Control run to Class 1,
850 and both Class 2 and Class 5 sediments to Class 2. That is, there were no pre-existing
851 Pearl River-derived sediments in the model domain when Cycle2 started. The results
852 of Cycle2 show that the retention in the "Proximal" and "Western" regions decreased
853 by 0.13% and 0.03% of the annual riverine sediment load, respectively, while the
854 retention in the "Eastern", "Southeastern", "Southern", "Southwestern", "Gulf", and
855 "Distal" regions increased by 0.03%, 0.03%, 0.01%, 0.02%, 0.07%, and 0.01%,
856 respectively. This indicates that the impact of this uncertainty in the proportion of bed
857 sediment grain sizes is relatively small.

858 Choosing an appropriate settling velocity may be more important than the
859 seasonal variation of critical shear stress for erosion. The results of the DSV case
860 show that a sediment settling velocity twice that of the Control run leads to the highest
861 retention in the "Proximal" and "Western" regions across all experiments (Figure 12e),
862 while reducing the retention in the "Distal" region. Although the settling velocity we
863 adopted is based on previous studies (Xia et al., 2004;Ralston et al., 2012) and model
864 calibrations (Figures S7c and S8e-f), with due consideration given to the presence of
865 slow-settling single fine grains and high-settling flocs in riverine sediments, certain

discrepancies might still exist in this setting. These discrepancies are contingent upon the actual magnitude of the low settling velocity of fine grains. In almost all cases, all flocs are retained in the "Proximal" region, and only in the Cycle case, flocs accounting for 0.01% of the annual load are retained in the "Western" region west of the "Proximal" region, indicating that high-settling flocs hardly leave the vicinity of the PRE. This finding shows close alignment with, yet exhibits minor distinctions from, the observed patterns in the Mekong Estuary (Xue et al., 2012). Xue et al. (2012) found that while the preponderance of flocs is deposited on the Mekong delta front precisely at the river mouth, a quantity equivalent to 1.6% of the annual riverine sediment load of flocs is deposited on the downdrift delta front further downstream from the river mouth. This is mainly because the estuary bay of the PRE is wider and there are numerous islands near the river mouth. The overwhelming majority of flocs are either deposited within the estuarine bay or captured by the surrounding islands. In conclusion, our results are affected by the settling velocity of fine grains. More field observations and studies on model parameterization regarding the settling velocity of fine grains are urgently needed.

As previously noted, we classified riverine sediments into two categories based on established research: 40% slow-settling fine grains and 60% fast-settling flocs. This 40%/60% distribution is consistent with the setting from earlier studies (Zhang et al., 2019;Zhang et al., 2021), as summarized in Table 1. While such assumptions are necessary for modeling purposes, the actual composition of riverine sediments in natural environments remains uncertain. To evaluate the sensitivity of our results to

888 this uncertainty, we conducted a conceptual analysis. If all riverine sediments were
889 hypothetically composed entirely of fast-settling flocs, they would be completely
890 retained near the source, with no transport to the Beibu Gulf. However, this scenario
891 is inconsistent with the radionuclide measurements obtained from Beibu Gulf surface
892 sediment samples (Lin et al., 2020). On the other hand, if all sediments were
893 considered slow-settling fine grains, only 16.13% would be retained proximally under
894 normal conditions (or 28.9% in the DSV case), a result that diverges significantly
895 from established research. Chen et al. (2023) analyzed high-resolution seismic data
896 and demonstrated that approximately 35% of the Pearl River-derived sediment has
897 been transported to offshore shelf areas over the past 6,500 years, suggesting that 65%
898 was deposited proximally. Our findings are in close agreement, indicating that 66.45%
899 of the Pearl River sediments are retained in the proximal region, while 33.55% are
900 transported elsewhere. This consistency with Chen et al. (2023) supports the validity
901 of our approach. Taken together, these analyses confirm that the 40%/60% fraction
902 assumption is a reasonable approximation for modeling purposes.

903 Furthermore, our model results demonstrate reasonable reliability in other aspects.
904 Liu et al. (2009) and Ge et al. (2014) using chirp sonar profiles from the inner shelf of
905 the South China Sea combined with Zong et al. (2009)'s onshore borehole data, found
906 that the thickness of Pearl River-derived sediments within the PRE since the Holocene
907 is over 20 m, while the mud thickness in the shallow waters west of the Chuanshan
908 Islands is approximately 5-10 m. Our calculated annual sediment thicknesses for these
909 two regions are approximately 2 mm and 0.3 mm (Figure 7d), respectively. Given our

910 model's annual riverine sediment load of 34.52 megatons—significantly reduced due
911 to recent human activities (Dai et al., 2008)—compared to the widely accepted
912 Holocene average of around 90 megatons (Liu et al., 2009), we estimate the total
913 sediment thickness over the past 7500 years to be roughly 39 meters and 6 meters for
914 these depositional zones, consistent with previous studies (Liu et al., 2009;Zong et al.,
915 2009).

916 Furthermore, our results reveal that 8.86% of the riverine sediment derived from
917 the Pearl River is transported to the Beibu Gulf (Figure 7c), primarily during the
918 winter season (Figure 7b). This finding not only confirms the earlier speculation
919 proposed by Ge et al. (2014) but also supplements the conclusions drawn by Lin et al.
920 (2020). From a hydrodynamic perspective, Shi et al. (2002) found that the net flux of
921 currents in the Qiongzhou Strait is westward throughout the year. Our results for both
922 wet summer (Figures 5a-b) and dry winter currents (Figures 6a-b) in the Qiongzhou
923 Strait are consistent with Shi et al. (2002). This westward flow contributes to the
924 westward transport of Pearl River sediment to the Beibu Gulf.

925 ## 4.2 Implications of our model results

926 The fate of sediment dispersed from the river into the coastal ocean involves at
927 least four processes: supply via plumes; initial deposition; resuspension and transport
928 by marine processes; and long-term net accumulation (Wright and Nittrouer, 1995). In
929 general, a significant proportion of river sediment tends to deposit in the estuary and
930 its vicinity (Walsh and Nittrouer, 2009;Hanebuth et al., 2015).

931 Walsh and Nittrouer (2009) present a hierarchical decision tree designed to

predict the marine dispersal system at a river mouth based on fundamental oceanographic and morphological characteristics. Within this framework, the fate of riverine sediment deposition can be determined using key factors, including riverine sediment discharge (greater or less than 2 megatons), shelf width (greater or less than 12 km), and wave and tidal range conditions (greater or less than 2 m) (Walsh and Nittrouer, 2009).

We aim to analyze our PRE simulation results using the framework established by Walsh and Nittrouer (2009). Although the Pearl River's riverine sediment discharge (Figure 2a) exceeds the Walsh and Nittrouer (2009)'s 2 megatons per year threshold, most of the sediment still remains deposited near the estuary (Figure 7c), indicating an estuarine accumulation-dominated (EAD) system, unlike the hierarchical decision tree proposed by Walsh and Nittrouer (2009). Outside the estuary, the continental shelf, spanning 200-220 km in width (Liu et al., 2014), significantly exceeds Walsh and Nittrouer (2009)'s 12 km threshold. As a result, most escaped riverine sediments tend to accumulate on the shelf rather than being captured by submarine canyons (Figures 7c-d). This wide, shallow shelf promotes sediment deposition and limits the direct transport of fine sediments into deeper waters (Walsh and Nittrouer, 2009). Subsequently, given that the annual mean tidal range (Chen et al., 2016;Gong et al., 2018b) and Hsig (Figure 3d) near the PRE are both below the 2 m threshold established by Walsh and Nittrouer (2009), the majority of escaped riverine sediments are predominantly deposited in the proximal depo-center.Our findings demonstrate that most of our outcomes are consistent with the hierarchical

decision tree proposed by Walsh and Nittrouer (2009), except for the application of the 2 megatons per year threshold for riverine sediment discharge. This phenomenon can primarily be attributed to the unique geomorphological characteristics of the PRE, including its broad mouth (Figures 1 and S1), extensive accommodation space encompassing approximately 2385 km^2 of water area (Wu et al., 2018), the presence and sheltering effect of numerous adjacent islands (Li et al., 2024b), and the division of fluvial sediment discharge through eight distinct outlets (Hu et al., 2011).

The monsoonal nature of the northern SCS (Figures 4a-b) induces pronounced seasonal variations in Pearl River-derived sediment transport and deposition (Figures 5 and 6). During the summer wet season, the Pearl River delivers approximately 95.17% of its annual sediment load to the PRE and the adjacent shelf (Figure 7a) under relatively calm wind and wave conditions (first column of Figure 4), leading to predominant proximal deposition (Figure 5f). In contrast, the winter dry season is characterized by strong northeasterly monsoon winds that generate high-energy waves (second column of Figure 4), significantly increasing bottom shear stress (Figures 4g-h). This process resuspends previously deposited sediments and facilitates their redistribution, particularly toward regions such as the Beibu Gulf (Figure 6f).

The PRE exhibits distinctive geomorphological features, yet its fine-grained sediment transport on the continental shelf conforms to general patterns observed in other monsoon-influenced estuarine systems. Similar multiple-stage sediment delivery and dispersal mechanisms have been documented in various major estuaries, including the Yellow River Estuary (Bian et al., 2013;Zeng et al., 2015), Changjiang

River Estuary (Zeng et al., 2015), and Mekong River Estuary (Xue et al., 2012;Eidam et al., 2017), demonstrating comparable sedimentary processes under monsoon climatic influences. In these systems, sediment transport is not confined to a single process but rather occurs in stages, influenced by seasonal variations in hydrodynamic conditions. Like the PRE, the Mekong experiences distinct phases of sediment deposition, with fine sediments being delivered during periods of high river discharge and then redistributed by waves and tidal forces, particularly during monsoonal shifts (Xue et al., 2012;Eidam et al., 2017). These complex patterns highlight the interplay between riverine inputs, coastal morphology, and oceanographic processes in shaping sediment dynamics.

These sediment delivery patterns have implications beyond sediment fate, particularly for carbon cycling. Sediment deposition in coastal and shelf areas plays a significant role in trapping organic carbon, influencing long-term carbon burial rates (LaRowe et al., 2020). Sediment dynamics directly influence the fate of organic carbon (OC) in marine environments, where sediments function as both a sink and a source of OC, playing a pivotal role in global carbon cycling (Repasch et al., 2021). The multiple-step transport mechanisms can lead to varying carbon storage locations, affecting the sequestration potential of these systems. Additionally, resuspension and redistribution of sediments, especially during high-energy events, may expose previously buried organic material, leading to carbon remineralization and influencing coastal nutrient cycles and ecosystem health (Ståhlberg et al., 2006;Moriarty et al., 2018). Therefore, understanding these patterns is crucial for assessing the broader

998 impacts on carbon cycling and coastal biogeochemical processes.

999 Furthermore, we evaluated the contributions of different physical processes by
1000 comparing the Control run with sensitivity cases. Our analysis reveals distinct roles of
1001 tidal forces, wave action, and background circulation in governing the transport and
1002 deposition of Pearl River-derived sediments (Figures 8, 9, 11a-c, and 12a-c).

1003 Tidal dynamics predominantly influence sediment behavior within the PRE.
1004 Neglecting tidal effects leads to an underestimation of bottom shear stress within the
1005 estuary (Figures 8a-b), resulting in an overestimation of sediment deposition (Figure
1006 11a) and consequently underestimating distal sediment retention (Figure 12a).

1007 Wave activity primarily controls sediment resuspension in three critical
1008 dimensions: (1) the river mouth, (2) the eastern and western nearshore regions outside
1009 the estuary, and (3) periods characterized by high wave energy during winter (Figures
1010 9c-d). The exclusion of wave effects results in overestimated sediment deposition in
1011 these areas and periods (Figure 11b), ultimately leading to an underestimation of
1012 sediment accumulation thickness in the Beibu Gulf (Figure 11b).

1013 Background circulation exerts its most significant influence during the summer
1014 months (Figure 5a vs. Figure 9e). The strong northeastward background current in
1015 summer serves as the primary driver for transporting Pearl River-derived sediments to
1016 the continental shelf east of the PRE. When considering only the weak southerly
1017 winds without the northeastward background current, merely 0.84% of Pearl River
1018 sediments are transported to the eastern shelf, substantially overestimating distal
1019 deposition (Figure 12c).

4.3 Limitations and Future Work

This study focuses on analyzing simulation results from a typical year, encompassing both wet and dry seasons from 2017 to 2018, to understand the seasonal variations and annual patterns of suspension, transport, and deposition of sediment in the PRE and adjacent shelf. However, it's essential to recognize that the long-term sediment transport and deposition dynamics in the Pearl River are influenced by numerous complex factors. These include changes in sea level and coastal line (Church and White, 2006;Harff et al., 2010;Hong et al., 2020), alterations in wind field and precipitation (Ning and Qian, 2009;Young et al., 2011), natural sedimentation within the Pearl River Delta (Wu et al., 2010), modifications in sediment load and underwater volume of the estuary caused by anthropogenic impact (Wu et al., 2014;Wu et al., 2018;Lin et al., 2022). Therefore, while this study sheds light on seasonal and annual timescale patterns, it cannot fully represent the short or long-term transport and deposition trends of the Pearl River sediment. Yet for many shelf systems, a lot of the sediment transport happens during short-lived events. Consideration of the episodicity of transport would be helpful for future studies.

Additionally, it's important to note that this article primarily focuses on the fate of the Pearl River sediment on the inner shelf. However, there are other smaller rivers within the Pearl River plume's expansion range, like the Han River, Rong River, Moyang River, Jian River, and Nandu River (Liu et al., 2016). Although these rivers contribute less freshwater and sediment compared to the Pearl River, they still impact seawater salinity, suspended sediment concentration, and seabed geomorphology

(Wang et al., 2023;Zong et al., 2024). Hence, there is a need for further systematic research to understand the processes and impacts of these smaller rivers comprehensively.

Lastly, while the model used in this study has shown good validation results, conducting more sensitivity experiments on sediment parameters, such as settling velocity and critical shear stress for erosion, would be beneficial. Settling velocity can influence the location of sediment depocenters, with higher settling velocities leading to more proximal entrapment and vice versa (Ralston and Geyer, 2017). Similarly, critical erosion stress can affect the resuspension of deposited sediment, with higher critical erosion stress resulting in less resuspension and more deposition especially during neap tides and weak wind wave events (Dong et al., 2020;Choi et al., 2023). Conducting such sensitivity analyses would enhance our understanding of sediment dynamics in estuaries and shelves. Besides, the model does not account for cohesive processes, such as consolidation and flocculation, which can significantly impact sediment behavior (Sherwood et al., 2018). Our model does not incorporate wave and current-supported gravity flows, which are important factors influencing sediment transport in submarine canyon areas (Harris et al., 2005;Ma et al., 2010;Zhang et al., 2020). Since our study area primarily focuses on the continental shelf and the simulated results indicate that sediment transport occurs mainly in the shallow inner shelf, where canyons are relatively rare, this omission has a relatively minor impact on our results.

5. Conclusions

This study utilizes the COAWST model to quantitatively analyze the seasonal suspension, transport, and annual fate of Pearl River-derived sediment on the continental shelf over a typical year, capturing key marine variables such as water level, wave height, flow velocity, salinity, temperature, and SSC.

The monsoonal nature of the northern SCS (Figures 4a-b) induces pronounced seasonal variations in Pearl River-derived sediment transport and deposition (Figures 5 and 6). During the wet summer, calm conditions foster initial sediment deposition via the river plume (Figures 5 and 7a). Conversely, winter's stronger winds and waves resuspend and transport sediments into Beibu Gulf, primarily during this dry season (Figures 6 and 7b). Our quantitative assessment reveals distinct spatial patterns in the annual fate of riverine sediments: approximately 66.45% of the total sediment load is retained within the estuarine vicinity, while 9.2% is deposited on the continental shelf east of the PRE. Furthermore, 8.86% and 10.3% of the sediment is transported to and retained in the Beibu Gulf and the area south of Hainan Island, respectively (Figure 7c).

Furthermore, we evaluated the contributions of different physical processes by comparing the Control run with the reduced-physics sensitivity experiments. Our analysis reveals distinct roles of tidal forces, wave action, and background circulation in governing the transport and deposition of Pearl River-derived sediments (Figures 8, 9, 11a-c, and 12a-c).

Tidal dynamics primarily govern sediment behavior in the PRE. Neglecting tides underestimates the bottom shear stress in the PRE (Figures 8a-b), overestimates

sediment deposition in the PRE (Figure 11a), and underestimates distal sediment retention (Figure 12a). Wave activity primarily controls sediment resuspension in three critical dimensions: (1) the river mouth, (2) the eastern and western nearshore regions outside the estuary, and (3) periods characterized by high wave energy during winter (Figures 9c-d). Excluding waves leads to overestimated sediment deposition in these areas and times (Figure 11b), underestimating accumulation in the Beibu Gulf (Figure 11b). Background circulation is most influential in summer (Figure 5a vs. Figure 9e), with a strong northeastward current transporting Pearl River-derived sediments to the eastern shelf. Without this current and under weak southerly winds, only 0.84% of sediments reach the eastern shelf, overestimating distal deposition (Figure 12c).The sediment model solutions are also highly sensitive to the parameterization of sediment characteristics and initial conditions (Figures 10, 11d-f, and 12d-f). Neglecting the need for a higher critical shear stress for erosion in winter overestimates resuspension and erosion on the shelf east of the Leizhou Peninsula during this season (Figure 10b), leading to a greater distal retention (Figure 12d). Increasing the settling velocity reduces SSC (Figures 10c-d) while overestimating the proximal retention and underestimating the distal retention (Figure 12e). Additionally, the model solutions are influenced by sediment initial conditions. If the model domain initially includes a full year of Pearl River-derived sediment retention, re-running the simulation results in further transport of previously retained sediments from the Beibu Gulf to more distal areas. However, the model is relatively insensitive to the initial bed grain size distribution (Experiment Cycle2; see Section 4.1).

Acknowledgments

This research was funded by the National Natural Science Foundation of China (grant numbers 42306015 and 42276169), the China Postdoctoral Science Foundation (grant number 2023M743988). Wenping Gong is supported by the Southern Marine Science and Engineering Guangdong Laboratory (Zhuhai) (SML2023SP238). The authors would like to thank the crew of the R/V Changhe Ocean for their valuable contribution during collection of the field-data. We express our gratitude to the two anonymous reviewers for their valuable suggestions in enhancing and improving this article.

Data availability

The HYbrid Coordinate Ocean Model (HYCOM) outputs are from: http://hycom.org/hycom. The NCEP Climate Forecast System Version 2 (CFSv2) reanalysis data can be obtained at the following website: https://rda.ucar.edu/datasets/ds094.1/dataaccess/. The NOAA WAVEWATCH III global ocean wave model output fields can be downloaded from: ftp://polar.ncep.noaa.gov/pub/history/waves. Hourly water-level data observed at Quarry Bay station are provided by the Hong Kong Observatory website: https://www.hko.gov.hk/sc/tide/marine/realtide.htm?s=QUB&t=TABLE. Hourly water-level data from Zhapo and Qinglan stations, provided by the Flanders Marine Institute (VLIZ), are part of the UNESCO/IOC Global Sea Level Observing System (GLOSS) and accessible at http://www.ioc-sealevelmonitoring.org. The mooring data for the M1 and M2 stations are sourced from Liu et al. (2023) and Li et al. (2024a).

The figure data and model configuration files used in this paper can be downloaded from: https://doi.org/10.5281/zenodo.15013448.

Declaration of Competing interests

The authors declare that they have no known competing financial interests or personal relationships that could have appeared to influence the work reported in this paper.

CRediT authorship contribution statement

Guang Zhang: Conceptualization, Numerical modeling, Validation, Data visualization, Writing-original draft, and Funding acquisition. **Suan Hu:** Writing-review & editing, Validation. **Xiaolong Yu:** Writing-review & editing. **Heng Zhang:** Writing-review & editing. **Wenping Gong:** Writing-review & editing, and Funding acquisition

Supplement:

We have included the validations and analysis of the model's water levels, Hsig, flow velocities, salinity, temperature, and SSC in the Supplement.

References

Bever, A. J., Harris, C. K., Sherwood, C. R., and Signell, R. P.: Deposition and flux of sediment from the Po River, Italy: An idealized and wintertime numerical modeling study, Marine Geology, 260, 69-80, 10.1016/j.margeo.2009.01.007, 2009.

Bever, A. J., and MacWilliams, M. L.: Simulating sediment transport processes in San Pablo Bay using coupled hydrodynamic, wave, and sediment transport models, Marine Geology, 345, 235-253, 10.1016/j.margeo.2013.06.012, 2013.

Bian, C., Jiang, W., and Greatbatch, R. J.: An exploratory model study of sediment transport sources and deposits in the Bohai Sea, Yellow Sea, and East China Sea, Journal of Geophysical Research:

Oceans, 118, 5908-5923, https://doi.org/10.1002/2013JC009116, 2013.

Booij, N., Ris, R. C., and Holthuijsen, L. H.: A third-generation wave model for coastal regions: 1. Model description and validation, Journal of Geophysical Research: Oceans, 104, 7649-7666, https://doi.org/10.1029/98JC02622, 1999.

Brand, A., Lacy, J. R., Hsu, K., Hoover, D., Gladding, S., and Stacey, M. T.: Wind-enhanced resuspension in the shallow waters of South San Francisco Bay: Mechanisms and potential implications for cohesive sediment transport, Journal of Geophysical Research, 115, 10.1029/2010jc006172, 2010.

Burchard, H., Schuttelaars, H. M., and Ralston, D. K.: Sediment Trapping in Estuaries, Annual Review of Marine Science, 10, 371-395, 10.1146/annurev-marine-010816-060535, 2018.

Cao, L., Liu, J., Shi, X., He, W., and Chen, Z.: Source-to-sink processes of fluvial sediments in the northern South China Sea: Constraints from river sediments in the coastal region of South China, Journal of Asian Earth Sciences, 185, 104020, 10.1016/j.jseaes.2019.104020, 2019.

Cao, Z., Ren, J., Deng, Z., Ye, L., and Wu, J.: Small-scale spatial variability in erosion threshold and bedform for cohesive sediment measured by 3D Sonar, Journal of Hydrology, 650, 132513, 10.1016/j.jhydrol.2024.132513, 2025.

Chapman, D. C.: Numerical Treatment of Cross-Shelf Open Boundaries in a Barotropic Coastal Ocean Model, Journal of Physical Oceanography, 15, 1060-1075, 1985.

Charnock, H.: Wind stress on a water surface, Quarterly Journal of the Royal Meteorological Society, 81, 639-640, https://doi.org/10.1002/qj.49708135027, 1955.

Chassignet, E. P., Hurlburt, H. E., Smedstad, O. M., Halliwell, G. R., Hogan, P. J., Wallcraft, A. J., Baraille, R., and Bleck, R.: The HYCOM (HYbrid Coordinate Ocean Model) data assimilative system, Journal of Marine Systems, 65, 60-83, https://doi.org/10.1016/j.jmarsys.2005.09.016, 2007.

Chen, S.-N., Geyer, W. R., Sherwood, C. R., and Ralston, D. K.: Sediment transport and deposition on a river-dominated tidal flat: An idealized model study, Journal of Geophysical Research, 115, 10.1029/2010jc006248, 2010.

Chen, Y., Deng, B., Saito, Y., Wang, Z., Yang, X., and Wu, J.: Pearl River sediment dispersal over its associated delta–estuary–shelf system during the Holocene, Sedimentology, 70, 2331-2354,

10.1111/sed.13123, 2023.

Chen, Z., Pan, J., and Jiang, Y.: Role of pulsed winds on detachment of low salinity water from the Pearl River Plume Upwelling and mixing processes, Journal of Geophysical Research: Oceans, 121, 2769-2788, 10.1002/2015JC011337, 2016.

Chen, Z., Gong, W., Cai, H., Chen, Y., and Zhang, H.: Dispersal of the Pearl River plume over continental shelf in summer, Estuarine, Coastal and Shelf Science, 194, 252-262, 10.1016/j.ecss.2017.06.025, 2017a.

Chen, Z., Pan, J., Jiang, Y., and Lin, H.: Far-reaching transport of Pearl River plume water by upwelling jet in the northeastern South China Sea, Journal of Marine Systems, 173, 60-69, 10.1016/j.jmarsys.2017.04.008, 2017b.

Chen, Z., Jiang, Y., Wang, J., and Gong, W.: Influence of a River Plume on Coastal Upwelling Dynamics: Importance of Stratification, Journal of Physical Oceanography, 49, 2345-2363, 10.1175/jpo-d-18-0215.1, 2019.

Cheng, P., Li, M., and Li, Y.: Generation of an estuarine sediment plume by a tropical storm, Journal of Geophysical Research: Oceans, 118, 856-868, 10.1002/jgrc.20070, 2013.

Chi, Y., and Rong, Z.: Effects of Breaking and Non -Breaking Surface W
Changjiang River Plume Dynamics in Summer, Journal of Geophysical Research: Oceans, 128, 10.1029/2022jc019501, 2023.

Choi, S. M., Seo, J. Y., and Ha, H. K.: Contribution of local erosion enhanced by winds to sediment transport in intertidal flat, Marine Geology, 465, 107171, 10.1016/j.margeo.2023.107171, 2023.

Church, J. A., and White, N. J.: A 20th century acceleration in global sea-level rise, Geophysical Research Letters, 33, n/a-n/a, 10.1029/2005gl024826, 2006.

Dai, S. B., Yang, S. L., and Cai, A. M.: Impacts of dams on the sediment flux of the Pearl River, southern China, Catena, 76, 36-43, 10.1016/j.catena.2008.08.004, 2008.

Dong, H., Jia, L., He, Z., Yu, M., and Shi, Y.: Application of parameters and paradigms of the erosion and deposition for cohesive sediment transport modelling in the Lingdingyang Estuary, China, Applied Ocean Research, 94, 101999, 10.1016/j.apor.2019.101999, 2020.

Dong, L., Su, J., Wong, L., Cao, Z., and Chen, J.: Seasonal variation and dynamics of the Pearl River plume, Continental Shelf Research, 24, 1761-1777, 10.1016/j.csr.2004.06.006, 2004.

1212 Drennan, W. M., Taylor, P. K., and Yelland, M. J.: Parameterizing the sea surface roughness, Journal of
1213 Physical Oceanography, 35, 835-848, Doi 10.1175/Jpo2704.1, 2005.
1214 Dyer, K. R.: Estuaries: A Physical Introduction, 2nd Edition, John Wiley & Sons, Chichester, 195 pp.,
1215 1997.
1216 Egbert, G. D., and Erofeeva, S. Y.: Efficient inverse Modeling of barotropic ocean tides, Journal of
1217 Atmospheric and Oceanic Technology, 19, 183-204, Doi
1218 10.1175/1520-0426(2002)019<0183:Eimobo>2.0.Co;2, 2002.
1219 Eidam, E. F., Nittrouer, C. A., Ogston, A. S., DeMaster, D. J., Liu, J. P., Nguyen, T. T., and Nguyen, T.
1220 N.: Dynamic controls on shallow clinoform geometry: Mekong Delta, Vietnam, Continental Shelf
1221 Research, 147, 165-181, 10.1016/j.csr.2017.06.001, 2017.
1222 Fairall, C. W., Bradley, E. F., Rogers, D. P., Edson, J. B., and Young, G. S.: Bulk parameterization of
1223 air-sea fluxes for Tropical Ocean-Global Atmosphere Coupled-Ocean Atmosphere Response
1224 Experiment, Journal of Geophysical Research: Oceans, 101, 3747-3764,
1225 https://doi.org/10.1029/95JC03205, 1996.
1226 Flather, R. A.: A tidal model of the north-west European continental shelf, Memoires Societe Royale
1227 des Sciences de Liege, 10, 141-164, 1976.
1228 Gan, J., Cheung, A., Guo, X., and Li, L.: Intensified upwelling over a widened shelf in the northeastern
1229 South China Sea, Journal of Geophysical Research, 114, 10.1029/2007jc004660, 2009.
1230 Gan, J., San Ho, H., and Liang, L.: Dynamics of Intensified Downwelling Circulation over a Widened
1231 Shelf in the Northeastern South China Sea, Journal of Physical Oceanography, 43, 80-94,
1232 10.1175/jpo-d-12-02.1, 2013.
1233 Gao, S., and Collins, M. B.: Holocene sedimentary systems on continental shelves, Marine Geology,
1234 352, 268-294, 10.1016/j.margeo.2014.03.021, 2014.
1235 Gao, X., Chen, S., Xie, X., Long, A., and Ma, F.: Non-aromatic hydrocarbons in surface sediments near
1236 the Pearl River estuary in the South China Sea, Environmental Pollution, 148, 40-47,
1237 10.1016/j.envpol.2006.11.001, 2007.
1238 Gao, X., Arthur Chen, C.-T., Wang, G., Xue, Q., Tang, C., and Chen, S.: Environmental status of Daya
1239 Bay surface sediments inferred from a sequential extraction technique, Estuarine, Coastal and
1240 Shelf Science, 86, 369-378, 10.1016/j.ecss.2009.10.012, 2010.

Ge, Q., Liu, J. P., Xue, Z., and Chu, F.: Dispersal of the Zhujiang River (Pearl River) derived sediment in the Holocene, Acta Oceanologica Sinica, 33, 1-9, 10.1007/s13131-014-0407-8, 2014.

Ge, Q., Xue, Z., Yao, Z., Zang, Z., and Chu, F.: Anti-phase relationship between the East Asian winter monsoon and summer monsoon during the Holocene?, Journal of Ocean University of China, 16, 175-183, 10.1007/s11802-017-3098-x, 2017.

Ge, Q., Xu, D., Ye, L., Yang, K., and Yao, Z.: Linking Monsoon Activity with River-Derived Sediments Deposition in the Northern South China Sea, Journal of Ocean University of China, 18, 1098-1104, 10.1007/s11802-019-4155-4, 2019.

Geyer, W. R., Hill, P. S., and Kineke, G. C.: The transport, transformation and dispersal of sediment by buoyant coastal flows, Continental Shelf Research, 24, 927-949, 10.1016/j.csr.2004.02.006, 2004.

Gong, W., Chen, Y., Zhang, H., and Chen, Z.: Effects of Wave–Current Interaction on Salt Intrusion During a Typhoon Event in a Highly Stratified Estuary, Estuaries and Coasts, 41, 1904-1923, 10.1007/s12237-018-0393-8, 2018a.

Gong, W., Lin, Z., Chen, Y., Chen, Z., Shen, J., and Zhang, H.: Effect of waves on the dispersal of the Pearl River plume in winter, Journal of Marine Systems, 186, 47-67, 10.1016/j.jmarsys.2018.05.003, 2018b.

Haidvogel, D. B., Arango, H., Budgell, W. P., Cornuelle, B. D., Curchitser, E., Di, L. E., Fennel, K., Geyer, W. R., Hermann, A. J., Lanerolle, L., Levin, J., McWilliams, J. C., Miller, A. J., Moore, A. M., Powell, T. M., Shchepetkin, A. F., Sherwood, C. R., Signell, R. P., Warner, J. C., and Wilkin, J.: Ocean forecasting in terrain-following coordinates: Formulation and skill assessment of the Regional Ocean Modeling System, Journal of Computational Physics, 227, 3595-3624, 10.1016/j.jcp.2007.06.016, 2008.

Hanebuth, T. J. J., Lantzsch, H., and Nizou, J.: Mud depocenters on continental shelves—appearance, initiation times, and growth dynamics, Geo-Marine Letters, 35, 487-503, 10.1007/s00367-015-0422-6, 2015.

Harff, J., Leipe, T., and Zhou, D.: Pearl River Estuary related sediments as response to Holocene climate change and anthropogenic impact (PECAI), Journal of Marine Systems, 82, S1-S2, 10.1016/j.jmarsys.2010.02.008, 2010.

Harris, C. K., Traykovski, P. A., and Geyer, W. R.: Flood dispersal and deposition by near -bed

gravitational sediment flows and oceanographic transport: A numerical modeling study of the Eel River shelf, northern California, Journal of Geophysical Research: Oceans, 110, 10.1029/2004jc002727, 2005.

Harris, C. K., Sherwood, C. R., Signell, R. P., Bever, A. J., and Warner, J. C.: Sediment dispersal in the northwestern Adriatic Sea, Journal of Geophysical Research, 113, 10.1029/2006jc003868, 2008.

Hong, B., Liu, Z., Shen, J., Wu, H., Gong, W., Xu, H., and Wang, D.: Potential physical impacts of sea-level rise on the Pearl River Estuary, China, Journal of Marine Systems, 201, 103245, 10.1016/j.jmarsys.2019.103245, 2020.

Horner-Devine, A. R., Hetland, R. D., and MacDonald, D. G.: Mixing and Transport in Coastal River Plumes, Annual Review of Fluid Mechanics, 47, 569-594, 10.1146/annurev-fluid-010313-141408, 2015.

Hu, J., Li, S., and Geng, B.: Modeling the mass flux budgets of water and suspended sediments for the river network and estuary in the Pearl River Delta, China, Journal of Marine Systems, 88, 252-266, 10.1016/j.jmarsys.2011.05.002, 2011.

Hu, S., Li, Y., Hu, P., Zhang, H., Zhang, G., and Gong, W.: The Impacts of Far -Field Typhoon -Generated Coastal T Sea: A Case Study of Typhoon In-Fa, Journal of Geophysical Research: Oceans, 129, 10.1029/2024jc021359, 2024.

Huang, D., Du, J., Deng, B., and Zhang, J.: Distribution patterns of particle-reactive radionuclides in sediments off eastern Hainan Island, China: Implications for source and transport pathways, Continental Shelf Research, 57, 10-17, 10.1016/j.csr.2012.04.019, 2013.

Jacob, R., Larson, J., and Ong, E.: M × N Communication and Parallel Interpolation in Community Climate System Model Version 3 Using the Model Coupling Toolkit, IJHPCA, 19, 293-307, 10.1177/1094342005056116, 2005.

Kirby, M. F., Devoy, B., Law, R. J., Ward, A., and Aldridge, J.: The use of a bioassay based approach to the hazard/risk assessment of cargo derived toxicity during shipping accidents: a case study--the MSC Napoli, Marine Pollution Bulletin, 56, 781-786, 10.1016/j.marpolbul.2008.01.006, 2008.

Krige, D. G.: A Statistical Approach to Some Basic Mine Valuation Problems on the Witwatersrand, Chemical, Metallurgical and Mining Society of South Africa, 1951.

Kuehl, S. A., Alexander, C. R., Blair, N. E., Harris, C. K., Marsaglia, K. M., Ogston, A. S., Orpin, A. R., Roering, J. J., Bever, A. J., Bilderback, E. L., Carter, L., Cerovski-Darriau, C., Childress, L. B., Reide Corbett, D., Hale, R. P., Leithold, E. L., Litchfield, N., Moriarty, J. M., Page, M. J., Pierce, L. E. R., Upton, P., and Walsh, J. P.: A source-to-sink perspective of the Waipaoa River margin, Earth-Science Reviews, 153, 301-334, 10.1016/j.earscirev.2015.10.001, 2016.

Kumar, N., Voulgaris, G., Warner, J. C., and Olabarrieta, M.: Implementation of the vortex force formalism in the coupled ocean-atmosphere-wave-sediment transport (COAWST) modeling system for inner shelf and surf zone applications, Ocean Modelling, 47, 65-95, 10.1016/j.ocemod.2012.01.003, 2012.

Lai, Z., Ma, R., Huang, M., Chen, C., Chen, Y., Xie, C., and Beardsley, R. C.: Downwelling wind, tides, and estuarine plume dynamics, Journal of Geophysical Research: Oceans, 121, 4245-4263, 10.1002/2015jc011475, 2016.

LaRowe, D. E., Arndt, S., Bradley, J. A., Estes, E. R., Hoarfrost, A., Lang, S. Q., Lloyd, K. G., Mahmoudi, N., Orsi, W. D., Shah Walter, S. R., Steen, A. D., and Zhao, R.: The fate of organic carbon in marine sediments - New insights from recent data and analysis, Earth-Science Reviews, 204, 103146, 10.1016/j.earscirev.2020.103146, 2020.

Larson, J., Jacob, R., and Ong, E.: The Model Coupling Toolkit: A New Fortran90 Toolkit for Building Multiphysics Parallel Coupled Models, IJHPCA, 19, 277-292, 2005.

Li, J., Li, M., and Xie, L.: Observations of near-inertial oscillations trapped at inclined front on continental shelf of the northwestern South China Sea, EGUsphere, 2024, 1-25, 10.5194/egusphere-2024-3909, 2024a.

Li, X., Chrysagi, E., Klingbeil, K., and Burchard, H.: Impact of Islands on Tidally Dominated River Plumes: A High-Resolution Modeling Study, Journal of Geophysical Research: Oceans, 129, e2023JC020272, https://doi.org/10.1029/2023JC020272, 2024b.

Li, Y., and Li, M.: Effects of winds on stratification and circulation in a partially mixed estuary, Journal of Geophysical Research, 116, 10.1029/2010jc006893, 2011.

Lin, S., Niu, J., Liu, G., Wei, X., and Cai, S.: Variations of suspended sediment transport caused by changes in shoreline and bathymetry in the Zhujiang (Pearl) River Estuary in the wet season, Acta Oceanologica Sinica, 41, 54-73, 10.1007/s13131-022-2017-1, 2022.

Lin, W., Feng, Y., Yu, K., Lan, W., Wang, Y., Mo, Z., Ning, Q., Feng, L., He, X., and Huang, Y.: Long-lived radionuclides in marine sediments from the Beibu Gulf, South China Sea: Spatial distribution, controlling factors, and proxy for transport pathway, Marine Geology, 424, 106157, 10.1016/j.margeo.2020.106157, 2020.

Liu, G., and Cai, S.: Modeling of suspended sediment by coupled wave-current model in the Zhujiang (Pearl) River Estuary, Acta Oceanologica Sinica, 38, 22-35, 10.1007/s13131-019-1455-3, 2019.

Liu, H., Ye, L., Zhou, W., and Wu, J.: Salt-wedge intrusion-retreat cycle induced sediment floc dynamics in bottom boundary layer (BBL) of a micro-tidal estuary, Marine Geology, 466, 107175, 10.1016/j.margeo.2023.107175, 2023.

Liu, J. P., Xue, Z., Ross, K., Yang, Z., and Gao, S.: Fate of Sediments Delivered to the Sea by Asian Large Rivers: Long-Distance Transport and Formation of Remote Alongshore Clinothems, Sediment. Rec., 7, 10.2110/sedred.2009.4.4, 2009.

Liu, Y., Gao, S., Wang, Y. P., Yang, Y., Long, J., Zhang, Y., and Wu, X.: Distal mud deposits associated with the Pearl River over the northwestern continental shelf of the South China Sea, Marine Geology, 347, 43-57, 10.1016/j.margeo.2013.10.012, 2014.

Liu, Z., Zhao, Y., Colin, C., Stattegger, K., Wiesner, M. G., Huh, C.-A., Zhang, Y., Li, X., Sompongchaiyakul, P., You, C.-F., Huang, C.-Y., Liu, J. T., Siringan, F. P., Le, K. P., Sathiamurthy, E., Hantoro, W. S., Liu, J., Tuo, S., Zhao, S., Zhou, S., He, Z., Wang, Y., Bunsomboonsakul, S., and Li, Y.: Source-to-sink transport processes of fluvial sediments in the South China Sea, Earth-Science Reviews, 153, 238-273, 10.1016/j.earscirev.2015.08.005, 2016.

Lu, X., Wang, Z., Guo, X., Gu, Y., Liang, W., and Liu, L.: Impacts of metal contamination and eutrophication on dinoflagellate cyst assemblages along the Guangdong coast of southern China, Marine Pollution Bulletin, 120, 239-249, 10.1016/j.marpolbul.2017.05.032, 2017.

Ma, Y., Friedrichs, C. T., Harris, C. K., and Wright, L. D.: Deposition by seasonal wave- and current-supported sediment gravity flows interacting with spatially varying bathymetry: Waiapu shelf, New Zealand, Marine Geology, 275, 199-211, https://doi.org/10.1016/j.margeo.2010.06.001, 2010.

Madsen, O. S.: Spectral Wave-Current Bottom Boundary Layer Flows, Coastal Engineering 1, 384-398, 1994.

Mao, Q., Shi, P., Yin, K., Gan, J., and Qi, Y.: Tides and tidal currents in the Pearl River Estuary, Continental Shelf Research, 24, 1797-1808, 10.1016/j.csr.2004.06.008, 2004.

McWilliams, J. C., Restrepo, J. M., and Lane, E. M.: An asymptotic theory for the interaction of waves and currents in coastal waters, Journal of Fluid Mechanics, 511, 135-178, 10.1017/s0022112004009358, 2004.

Meade, R. H.: Landward Transport of Bottom Sediments in Estuaries of the Atlantic Coastal Plain, Journal of Sedimentary Petrology, 39, 222-234, 1969.

Moriarty, J. M., Harris, C. K., Friedrichs, M. A. M., Fennel, K., and Xu, K.: Impact of Seabed Resuspension on Oxygen and Nitrogen Dynamics in the Northern Gulf of Mexico: A Numerical Modeling Study, Journal of Geophysical Research: Oceans, 123, 7237-7263, https://doi.org/10.1029/2018JC013950, 2018.

Ning, L., and Qian, Y.: Interdecadal change in extreme precipitation over South China and its mechanism, Advances in Atmospheric Sciences, 26, 109-118, 10.1007/s00376-009-0109-x, 2009.

Nittrouer, C. A., and Wright, L. D.: Transport of particles across continental shelves, Reviews of Geophysics, 32, 85-113, https://doi.org/10.1029/93RG02603, 1994.

Orlanski, I.: A simple boundary condition for unbounded hyperbolic flows, Journal of Computational Physics, 21, 251-269, 10.1016/0021-9991(76)90023-1, 1976.

Ou, S., Zhang, H., and Wang, D.: Dynamics of the buoyant plume off the Pearl River Estuary in summer, Environmental Fluid Mechanics, 9, 471-492, 10.1007/s10652-009-9146-3, 2009.

Ralston, D. K., Geyer, W. R., and Warner, J. C.: Bathymetric controls on sediment transport in the Hudson River estuary: Lateral asymmetry and frontal trapping, Journal of Geophysical Research: Oceans, 117, 10.1029/2012jc008124, 2012.

Ralston, D. K., and Geyer, W. R.: Sediment Transport Time Scales and Trapping Efficiency in a Tidal River, Journal of Geophysical Research: Earth Surface, 122, 2042-2063, 10.1002/2017jf004337, 2017.

Raymond, W. H., and Kuo, H. L.: A radiation boundary condition for multi-dimensional flows, Quarterly Journal of the Royal Meteorological Society, 110, 535-551, 1984.

Repasch, M., Scheingross, J. S., Hovius, N., Lupker, M., Wittmann, H., Haghipour, N., Gröcke, D. R., Orfeo, O., Eglinton, T. I., and Sachse, D.: Fluvial organic carbon cycling regulated by sediment

transit time and mineral protection, Nature Geoscience, 14, 842-848, 10.1038/s41561-021-00845-7, 2021.

Rong, Z., Hetland, R. D., Zhang, W., and Zhang, X.: Current–wave interaction in the Mississippi–Atchafalaya river plume on the Texas–Louisiana shelf, Ocean Modelling, 84, 67-83, 10.1016/j.ocemod.2014.09.008, 2014.

Saha, S., Moorthi, S., Wu, X., Wang, J., Nadiga, S., Tripp, P., Behringer, D., Hou, Y.-T., Chuang, H.-y., Iredell, M., Ek, M., Meng, J., Yang, R., Mendez, M. P., van den Dool, H., Zhang, Q., Wang, W., Chen, M., and Becker, E.: The NCEP Climate Forecast System Version 2, Journal of Climate, 27, 2185-2208, https://doi.org/10.1175/JCLI-D-12-00823.1, 2014.

Sanford, L. P.: Wave-forced resuspension of upper Chesapeake Bay muds, Estuaries, 17, 148-165, 1994.

Shchepetkin, A. F., and McWilliams, J. C.: The regional oceanic modeling system (ROMS): a split-explicit, free-surface, topography-following-coordinate oceanic model, Ocean Modelling, 9, 347-404, https://doi.org/10.1016/j.ocemod.2004.08.002, 2005.

Shepard, F. P.: Nomenclature Based on Sand-silt-clay Ratios, Journal of Sedimentary Research, 24, 151-158, 1954.

Sherwood, C. R., Aretxabaleta, A. L., Harris, C. K., Rinehimer, J. P., Verney, R., and Ferré, B.: Cohesive and mixed sediment in the Regional Ocean Modeling System (ROMS v3.6) implemented in the Coupled Ocean–Atmosphere–Wave–Sediment Transport Modeling System (COAWST r1234), Geoscientific Model Development, 11, 1849-1871, 10.5194/gmd-11-1849-2018, 2018.

Shi, M., Chen, C., Xu, Q., Lin, H., Liu, G., Wang, H., Wang, F., and Yan, J.: The Role of Qiongzhou Strait in the Seasonal Variation of the South China Sea Circulation, Journal of Physical Oceanography, 32, 103-121, 2002.

Skamarock, W. C., Klemp, J. B., Dudhia, J., Gill, D. O., Barker, D. M., Wang, W., and Powers, J. G.: A Description of the Advanced Research WRF Version 2, 2005,

Smagorinsky, J.: GENERAL CIRCULATION EXPERIMENTS WITH THE PRIMITIVE EQUATIONS, Monthly Weather Review, 91, 99-164, 10.1175/1520-0493(1963)091<0099:gcewtp>2.3.co;2, 1963.

Song, Y., and Haidvogel, D.: A Semi-implicit Ocean Circulation Model Using a Generalized Topography-Following Coordinate System, Journal of Computational Physics, 115, 228-244, https://doi.org/10.1006/jcph.1994.1189, 1994.

Ståhlberg, C., Bastviken, D., Svensson, B. H., and Rahm, L.: Mineralisation of organic matter in coastal sediments at different frequency and duration of resuspension, Estuarine, Coastal and Shelf Science, 70, 317-325, https://doi.org/10.1016/j.ecss.2006.06.022, 2006.

Su, J.: Overview of the South China Sea circulation and its influence on the coastal physical oceanography outside the Pearl River Estuary, Continental Shelf Research, 24, 1745-1760, 10.1016/j.csr.2004.06.005, 2004.

Tolman, H., Accensi, M., Alves, J.-H., Ardhuin, F., Barbariol, F., Benetazzo, A., Bennis, A.-C., Bidlot, J., Booij, N., Boutin, G., Campbell, T., Chalikov, D., Chawla, A., Cheng, S., Collins Iii, C., Filipot, J.-F., Foreman, M., Janssen, P., Leckler, F., and Westhuysen, A.: User manual and system documentation of WAVEWATCH III (R) version 5.16, 2016.

Turner, A., and Millward, G. E.: Suspended Particles: Their Role in Estuarine Biogeochemical Cycles, Estuarine, Coastal and Shelf Science, 55, 857-883, 10.1006/ecss.2002.1033, 2002.

van der Wegen, M., Dastgheib, A., Jaffe, B. E., and Roelvink, D.: Bed composition generation for morphodynamic modeling: case study of San Pablo Bay in California, USA, Ocean Dynamics, 61, 173-186, 10.1007/s10236-010-0314-2, 2010.

Walsh, J. P., and Nittrouer, C. A.: Understanding fine-grained river-sediment dispersal on continental margins, Marine Geology, 263, 34-45, 10.1016/j.margeo.2009.03.016, 2009.

Wang, S., Zhang, N., Chen, H., Li, L., and Yan, W.: The surface sediment types and their rare earth element characteristics from the continental shelf of the northern south China sea, Continental Shelf Research, 88, 185-202, 10.1016/j.csr.2014.08.005, 2014.

Wang, S., Wu, S., Yan, W., Huang, W., Miao, L., Lu, J., Chen, Z., and Liu, F.: Rare metal elements in surface sediment from five bays on the northeastern coast of the South China Sea, Environmental Earth Sciences, 74, 4961-4971, 10.1007/s12665-015-4504-6, 2015.

Wang, S., Li, J., Wu, S., Yan, W., Huang, W., Miao, L., and Chen, Z.: The distribution characteristics of rare metal elements in surface sediments from four coastal bays on the northwestern South China Sea, Estuarine, Coastal and Shelf Science, 169, 106-118, 10.1016/j.ecss.2015.12.001, 2016.

Wang, Y., Wang, Y., Wan, X., Huang, C., Wang, R., Liu, X., Yi, J., and Zhang, Y.: Influence of the Hanjiang River's Inlet Sediment Decrease on Modern Sedimentation in the Underwater Delta, Applied Sciences, 13, 8039, 10.3390/app13148039, 2023.

Warner, J. C., Sherwood, C. R., Arango, H. G., and Signell, R. P.: Performance of four turbulence closure models implemented using a generic length scale method, Ocean Modelling, 8, 81-113, 10.1016/j.ocemod.2003.12.003, 2005.

Warner, J. C., Sherwood, C. R., Signell, R. P., Harris, C. K., and Arango, H. G.: Development of a three-dimensional, regional, coupled wave, current, and sediment-transport model, Computers & Geosciences, 34, 1284-1306, 10.1016/j.cageo.2008.02.012, 2008.

Warner, J. C., Armstrong, B., He, R., and Zambon, J. B.: Development of a Coupled Ocean–Atmosphere–Wave–Sediment Transport (COAWST) Modeling System, Ocean Modelling, 35, 230-244, 10.1016/j.ocemod.2010.07.010, 2010.

Warner, J. C., Schwab, W. C., List, J. H., Safak, I., Liste, M., and Baldwin, W.: Inner-shelf ocean dynamics and seafloor morphologic changes during Hurricane Sandy, Continental Shelf Research, 138, 1-18, 10.1016/j.csr.2017.02.003, 2017.

Weatherall, P., Marks, K. M., Jakobsson, M., Schmitt, T., Tani, S., Arndt, J. E., Rovere, M., Chayes, D., Ferrini, V., and Wigley, R.: A new digital bathymetric model of the world's oceans, Earth and Space Science, 2, 331-345, https://doi.org/10.1002/2015EA000107, 2015.

Wright, L. D., and Coleman, J. M.: Variations in Morphology of Major River Deltas as Functions of Ocean Wave and River Discharge Regimes, AAPG Bulletin, 57, 370-398, 1973.

Wright, L. D., and Nittrouer, C. A.: Dispersal of river sediments in coastal seas: Six contrasting cases, Estuaries, 18, 494-508, 10.2307/1352367, 1995.

Wu, C., Xing, W., Jie, R., Yun, B., Zhigang, H., Yiaping, L., Heyin, S., and Wenyan, Z.: Morphodynamics of the rock-bound outlets of the Pearl River estuary, South China — A preliminary study, Journal of Marine Systems, 82, S17-S27, 10.1016/j.jmarsys.2010.02.002, 2010.

Wu, Z., Milliman, J. D., Zhao, D., Zhou, J., and Yao, C.: Recent geomorphic change in LingDing Bay, China, in response to economic and urban growth on the Pearl River Delta, Southern China, Global and Planetary Change, 123, 1-12, 10.1016/j.gloplacha.2014.10.009, 2014.

Wu, Z., Milliman, J. D., Zhao, D., Cao, Z., Zhou, J., and Zhou, C.: Geomorphologic changes in the

lower Pearl River Delta, 1850–2015, largely due to human activity, Geomorphology, 314, 42-54, 10.1016/j.geomorph.2018.05.001, 2018.

Wu, Z. Y., Saito, Y., Zhao, D. N., Zhou, J. Q., Cao, Z. Y., Li, S. J., Shang, J. H., and Liang, Y. Y.: Impact of human activities on subaqueous topographic change in Lingding Bay of the Pearl River estuary, China, during 1955-2013, Scientific Reports, 6, 37742, 10.1038/srep37742, 2016.

Xia, X. M., Li, Y., Yang, H., Wu, C. Y., Sing, T. H., and Pong, H. K.: Observations on the size and settling velocity distributions of suspended sediment in the Pearl River Estuary, China, Continental Shelf Research, 24, 1809-1826, 10.1016/j.csr.2004.06.009, 2004.

Xue, Z., He, R., Liu, J. P., and Warner, J. C.: Modeling transport and deposition of the Mekong River sediment, Continental Shelf Research, 37, 66-78, 10.1016/j.csr.2012.02.010, 2012.

Yang, B., Liu, S.-M., and Zhang, G.-L.: Geochemical characteristics of phosphorus in surface sediments from the continental shelf region of the northern South China Sea, Marine Chemistry, 198, 44-55, 10.1016/j.marchem.2017.11.001, 2018.

Yang, J., Wu, D., and Lin, X.: On the dynamics of the South China Sea Warm Current, Journal of Geophysical Research: Oceans, 113, https://doi.org/10.1029/2007JC004427, 2008.

Yang, Y., Guan, W., Deleersnijder, E., and He, Z.: Hydrodynamic and sediment transport modelling in the Pearl River Estuary and adjacent Chinese coastal zone during Typhoon Mangkhut, Continental Shelf Research, 233, 104645, 10.1016/j.csr.2022.104645, 2022.

Young, I. R., Zieger, S., and Babanin, A. V.: Global trends in wind speed and wave height, Science, 332, 451-455, 10.1126/science.1197219, 2011.

Zeng, X., He, R., Xue, Z., Wang, H., Wang, Y., Yao, Z., Guan, W., and Warrillow, J.: River-derived sediment suspension and transport in the Bohai, Yellow, and East China Seas: A preliminary modeling study, Continental Shelf Research, 111, 112-125, https://doi.org/10.1016/j.csr.2015.08.015, 2015.

Zhang, G., Cheng, W., Chen, L., Zhang, H., and Gong, W.: Transport of riverine sediment from different outlets in the Pearl River Estuary during the wet season, Marine Geology, 415, 105957, 10.1016/j.margeo.2019.06.002, 2019.

Zhang, G., Chen, Y., Cheng, W., Zhang, H., and Gong, W.: Wave Effects on Sediment Transport and Entrapment in a Channel -Shoal Estuary: The

Journal of Geophysical Research: Oceans, 126, 10.1029/2020jc016905, 2021.

Zhang, J., Jiang, Q., Jeng, D., Zhang, C., Chen, X., and Wang, L.: Experimental Study on Mechanism of Wave-Induced Liquefaction of Sand-Clay Seabed, Journal of Marine Science and Engineering, 8, 66, 10.3390/jmse8020066, 2020.

Zhang, W., Wei, X., Zheng, J., Zhu, Y., and Zhang, Y.: Estimating suspended sediment loads in the Pearl River Delta region using sediment rating curves, Continental Shelf Research, 38, 35-46, 10.1016/j.csr.2012.02.017, 2012.

Zhang, W., Zheng, J., Ji, X., Hoitink, A. J. F., van der Vegt, M., and Zhu, Y.: Surficial sediment distribution and the associated net sediment transport pattern retain-->in the Pearl River Estuary, South China, Continental Shelf Research, 61-62, 41-51, 10.1016/j.csr.2013.04.011, 2013.

Zhong, Y., Chen, Z., Li, L., Liu, J., Li, G., Zheng, X., Wang, S., and Mo, A.: Bottom water hydrodynamic provinces and transport patterns of the northern South China Sea: Evidence from grain size of the terrigenous sediments, Continental Shelf Research, 140, 11-26, 10.1016/j.csr.2017.01.023, 2017.

Zong, X., Cheng, X., Zhang, S., Lian, Q., Deng, F., and Chen, Z.: Tidal effects on dynamics and freshwater transport of a medium-scale river plume with multiple outlets, Ocean Modelling, 188, 102338, https://doi.org/10.1016/j.ocemod.2024.102338, 2024.

Zong, Y., Huang, K., Switzer, A., yu, F., and Yim, W.: An evolutionary model for the Holocene formation of the Pearl River delta, China, The Holocene, 19, 129-142, 10.1177/0959683608098957, 2009.